Silver Nanoparticles:

From the production and restructuring in gas phase to the transfer and dissolution kinetics in the liquid

By

Fabian Schmidt-Ott

Master Thesis

SEPTEMBER 2020

Department of Environmental Engineering
TU DELFT

Research conducted under collaboration with
The Cyprus Institute (Nicosia, Cyprus)

Assessment committee:
Prof. Dr. George Biskos (chair)
Prof. Dr. Gabrie Meesters
Prof. Dr. William Ball

Abstract

The increasing use of silver nanoparticles (AgNPs) in various products leads to their presence in the aquatic environment. The dissolution of AgNPs is an important property that has a direct impact on human health and the natural environment. Understanding the dissolution behaviour of nanoparticles in liquid suspensions is essential for predicting their potential toxic effect in organisms, ranging from viruses and bacteria to humans. Moreover, the dissolution rate of nanoparticles can explain some of their disinfecting properties, which are important for sanitation.

The objective of this study is to determine the dissolution behaviour of AgNPs in pure water and to improve our understanding of its most fundamental principles. Dissolution constants of AgNPs found in literature span over a wide range, indicating that improvement of the measuring method is needed. AgNPs in this study were produced in a principally impurity-free way, from the gas phase, after which they were transferred into liquid solutions. The purity of the particles produced in this study is in principle higher compared to those used until now, which allows for higher precision in determining the dissolution constant. Measuring the silver ion concentration in the resulting liquid solutions (i.e., after introducing the AgNPs in the solution) with an ICP-MS at specific time intervals gave direct information on the dissolution kinetics. The experiments were repeated with particles having diameters from 7 to 12 nm and, as expected, dissolution kinetics were found to be highly dependent on particle size. The determined dissolution constants are in the same order of magnitude as the values reported in literature. To further improve the reliability of the measurements, the experiment needs to be repeated using different methods for transferring the particles into the liquid, given that the used bubbling method showed deficiencies.

Table of Contents

1. Introduction

Nanoparticles have found an increasing number of applications over recent years as they can enhance the performance of commercial, medical and industrial products, such as cosmetics, clothing, electronic devices, medicine and food packaging (Benn, Cavanagh, Hristovski, Posner, & Westerhoff, 2010). The global production of silver nanoparticles (AgNPs) is estimated at approximately 320 ton/year (Nowack, Krug, & Height, 2011). The increased use of nanoparticles inevitably leads to their release to the environment, which consequently increases the exposure of humans and other organisms to them (Dale et al., 2015).

Nanoparticles can be harmful to a wide range of organisms, such as microbes, algae, fungi, vertebrates, invertebrates and human cells (Levard, Hotze, Lowry, & Brown Jr, 2012). For humans, two main pathways exist through which nanoparticles can be taken up: through the respiratory or gastrointestinal system. In both cases, the dissolution kinetics of nanoparticles are relevant and affect the extent at which they exhibit toxic properties.

As is the case with most metal nanoparticles that are not made of noble materials, AgNPs dissolve once exposed to the wet environment, resulting in a nanoparticle-ion mixture (AgNPs + Ag^+). Ag^+ interacts with specific groups of proteins, which can result in the inactivation of vital enzymes and likely affects DNA replication (Zhang, Yao, Sullivan, & Chen, 2011). Besides the toxicity caused by the ions, AgNPs themselves can also be toxic due to their size and shape; e.g., by blocking and clogging narrow veins. The toxicity of nanoparticles therefore depends on both their physical and chemical properties. In order to obtain a clearer picture of nanotoxicity as a whole, it is important to draw a line between these two toxicity effects and study each of them separately. From the chemical point of view, the rate at which the particles dissolve is of importance, because the toxicity of any chemical - such as the silver ions from the nanoparticle - is strongly dependent on the concentration that the organism is exposed to. For better understanding nanotoxicity, it is therefore important to understand their dissolution kinetics and to quantify the factors that influence it.

A clear understanding of the dissolution mechanism of nanoparticles is not only important for toxicological studies, but is also relevant to some of their applications. AgNPs exhibit strong antimicrobial behaviour, which can be useful for disinfection purposes. Helmlinger et al. (2016) showed that nanoparticles with different sizes and shapes have the same cytotoxicity towards human cells, but a different toxicity towards bacteria. This size and shape dependency could make nanoparticles a promising means of eliminating bacteria in a controlled manner.

The dissolution rate of nanoparticles strongly depends both on their physical and chemical properties (e.g., size and composition), but also on the type of environment that they are exposed to (e.g., body fluid or river water). Previous studies show large disagreement on the dissolution behaviour of nanoparticles (see Table 4.1 in Chapter 4), which can be explained by the numerous factors that the dissolution kinetics depend on. The large discrepancies of previous studies show that better understanding of the dissolution behaviour from the basic level is required.

The goal of this research is to determine the dissolution rate of nanoparticles in pure, deionized water. Nanoparticles in this study are produced in the gas phase in a fundamentally different - presumably cleaner - way than any of the previous studies have done. Since the dissolution kinetics are expected to depend on particle size, the dissolution rate will be determined for different sizes of nanoparticles. The principles of production and characterization of nanoparticles in the gas phase will be explained in Chapter 2. Since particles are produced from the gas phase, one of the challenges is to transfer the nanoparticles from the gas into the liquid, without influencing their properties. Hence, Chapter 3 is devoted to a technique that was found to be most applicable for this purpose: the bubbling method. Finally, Chapter 4 focuses on the measurement of dissolution rate of nanoparticles of different sizes and the discussion of the results.

2. Nanoparticle production and characterization

2.1 Production

One method of producing nanoparticles is by spark ablation, see Fig. 2.1 (Schwyn, Garwin, & Schmidt-Ott, 1988). The method relies on the ablation of bulk material (in the form of electrodes) by the bombardment of high frequency sparks. Temperatures associated with the spark itself are above 10,000 K, which causes material on the surface of the electrode to immediately evaporate in the vicinity of the spark at areas of few micrometres (Reinmann & Akram, 1997). The evaporated atoms form a local cloud of plasma; a gas that consists of ions, neutral atoms and free electrons. While sparking, a constant flow of inert carrier gas (e.g. nitrogen, argon or helium) is passed through the gap between the electrodes, quenching the electrode material. Due to the relatively low temperature of this gas (25 °C), the plasma vapor instantaneously cools down, causing the vapor atoms to nucleate and subsequently condense on the formed nuclei. This condensation creates the smallest set of pure metal particles: atomic clusters, a collection of single atoms. The material of the electrode has to be good a conductor to establish a spark, therefore metals are the best candidates.

While the newly formed atomic clusters are carried downstream by the carrier gas, they inevitably grow larger due to random collisions with each other. This random clumping of particles is called coagulation. Interestingly, particles that result from initial coagulation of atomic clusters are perfectly spherical. This can be explained by the liquid-like behaviour that particles at these sizes have, as molecules inside the particle are not organized in a metallic structure yet (Buffat & Borel, 1976). Once the particles exceed the sizes at which they show liquid-like behaviour, they become part of larger aggregates, in which the constituents – called the primary particles – are sintered together. As these aggregates continue to coagulate, agglomerates are formed, which randomly adhere together through Van der Waals forces (Friedlander, 1977). Agglomerates therefore exist of primary particles that are randomly arranged in fractal structures, as shown in Fig. 2.1.

Using spark ablation, a constant stream of nanoparticles can be produced, which, depending on the operation conditions have diameters from the size of atomic clusters to some tens of nanometres. Besides the stable production rate, particles produced by the spark have high purity, consisting of a single metallic element (provided that no impurities are added in the subsequent tubing). A good fraction of the particles produced by spark ablation carry a positive or negative charge, which has the advantage that they can be easily classified according to their size using a Differential Particle Counter (DMA; see next section).

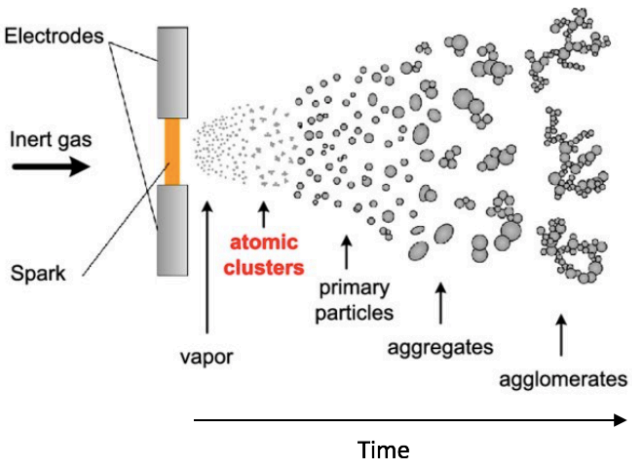

Fig. 2.1. States of the aerosol-vapor cloud produced by spark ablation (Pfeiffer, Feng, & Schmidt-Ott, 2014).

2.2 Characterization

Nanoparticles can be characterized according to various properties. The size and concentration of particles can be analysed either by off-line methods, e.g. by the deposition on a surface, followed by microscopy analysis (e.g. transmission electron microscope, TEM), or one can choose to characterize them while they are still suspended in the air. An important advantage of doing the latter is that it enables real-time measurement. The following paragraphs focus on the latter, in-situ characterization of nanoparticles.

2.2.1 Condensation Particle Counter

CPCs are commonly used for measuring the number concentration of aerosol particles. The counting technique is based on light-scattering measurement. In the optical chamber is a laser and opposite a photodetector with a shatter in between, as shown in the top of Fig. 2.2. Every time that a particle passes through the optical chamber, it scatters light to the photodetector, which results in a momentarily increase of signal. Counting the amounts of signals over time gives a representation of the number of particles passing the optical chamber per second (#/s). Knowing the flow rate in cm^3/s, the number concentration in $\#/cm^3$ can be derived (Hinds, 1999).

The counting of particles based on optical methods is only possible for sizes in the micron range (10^{-6} m), because smaller particles interact with light only weakly. Therefore, particles are grown to larger sizes once they enter the CPC. The sampled aerosol is first passed through a saturator tube in which it is saturated with the working fluid (butanol in most cases). Downstream, particles arrive to the condenser tube, where a sudden temperature decrease causes saturation levels to rise to supersaturated levels (Hinds, 1999). As Köhler's theory predicts, the supersaturations are sufficient to even grow particles of initial diameters of 3 nm to large enough sizes to be detected by the optical unit (TSI Inc., 2002; Köhler, 1936). Most particles, after passing through the saturator and condenser grow to final sizes around 10 µm. After the particles are detected, they are caught by a HEPA (High Efficiency Particulate Air) filter, which safely removes all sizes of particles from the aerosol.

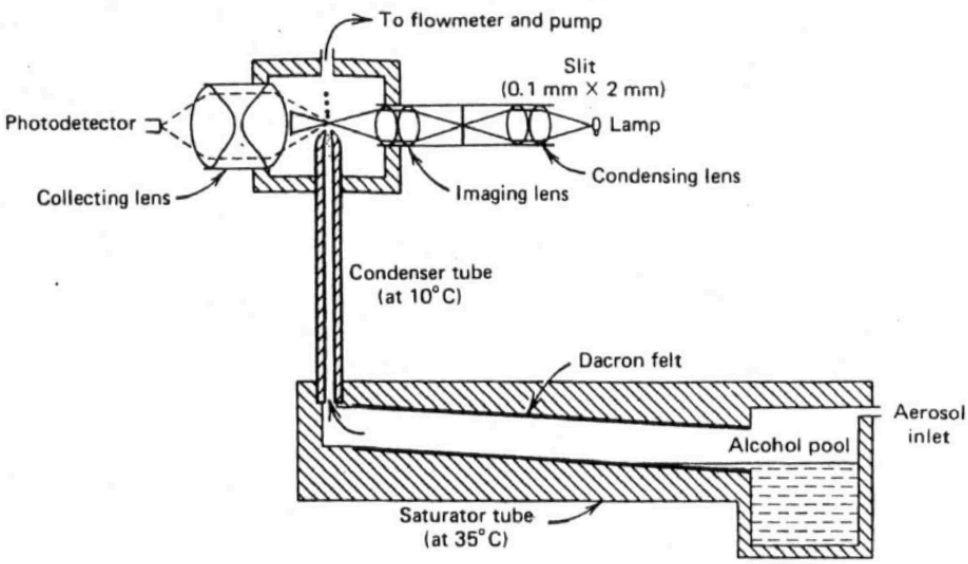

Fig. 2.2. Schematic diagram of a condensation particle counter (Hinds, 1999).

2.2.2 CPC Calibration

Calibration of the CPC is important when counting particles with sizes that are near to the lower detection limit. The efficiency at which a particle grows to detectable sizes degrades significantly as particles become smaller. Therefore, the CPC used in this experiment was calibrated against an electrometer, for which it is known that the detection efficiency does not depend on particle size (Maisser, 2011). Fig. 2.3 shows the curve that is obtained from a parallel measurement with a CPC and electrometer that measure the same monodisperse aerosol. This measurement was repeated for different particle sizes. Different sizes of monodisperse aerosol were obtained by size-selection with a DMA (the working principle of the DMA is explained in the next subchapter). The efficiency for each size is calculated from the ratio of measured number concentrations from the CPC and electrometer:

$$\eta_{CPC}(d_p) = \frac{N_{CPC}}{N_{EM}} \cdot 100\% \qquad \textit{(Eq. 2.1)}$$

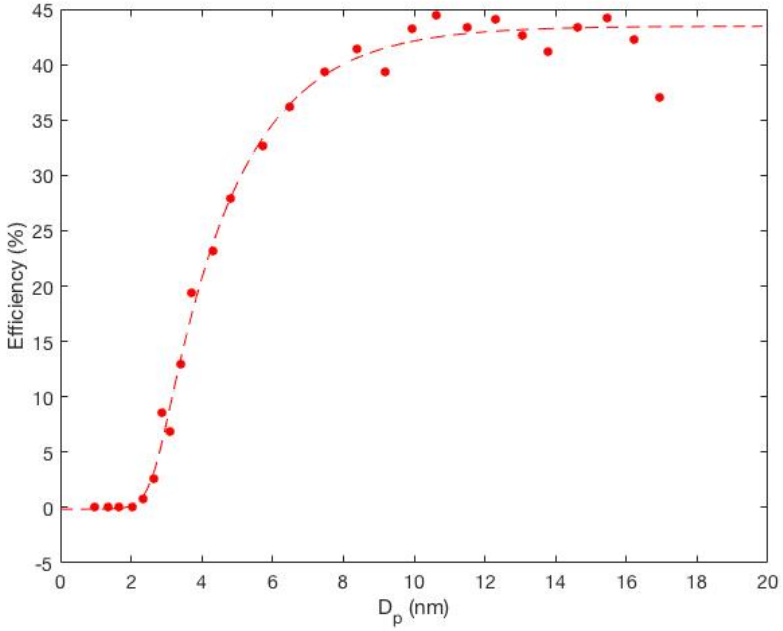

Fig. 2.3. Measured detection efficiency of CPC (TSI 3025a) for particle diameters in the nanoscale, using silver nanoparticles.

2.2.3 Differential Mobility Analyzer

For studying aerosol particles, it is often necessary to select certain particle sizes. This can be achieved using a Differential Mobility Analyser (DMA), in which particles are selected according to their electrical mobility Z_p defined by as:

$$Z_p = \frac{v}{E}, \qquad \textit{(Eq. 2.2)}$$

where v is the particle velocity that a charged particle acquires in an applied electric field (E). A particle moving inside an electric field at constant velocity experiences a drag force that is equal to the electrostatic force. This drag force is dependent on the particle's diameter (d_p) and

hence influences the particle's velocity inside the electric field. The particle's velocity is defined as:

$$v = \frac{neEC_C}{3\pi\eta d_p}, \qquad \textit{(Eq. 2.3)}$$

where n is the charge of the particle, e is the elementary charge, η is the dynamic viscosity of the gas and C_C is the Cunningham slip correction factor (Hinds, 1999). The latter is a factor that accounts for the slightly different drag force that a small particle experiences when it moves through a gas, as compared to larger particles in the submicron range. It can be imagined as the smaller particles "slipping" through the gas experiencing less resistance from the gas, since, due to their small sizes gas molecules don't collide with the particles at any given moment.

Substituting Eq. 2.3 in 2.2, gives a direct relationship between the electrical mobility and the diameter of the particle. Note that the diameter that is determined from the electrical mobility is the diameter of a particle equivalent to that of a spherical particle having the same electrical mobility. It is therefore strictly speaking the 'mobility diameter', but for simplicity will be referred to as the "particle diameter" (d_p) in the following.

Fig. 2.4 shows a schematic representation of a cylindrical DMA. The sampled aerosol enters at the top, together with a laminar sheath flow of clean air. High (negative) voltage is applied to the central rod, which induces an electric field perpendicular to the aerosol flow direction. Positively charged particles are attracted toward the negatively charged rod along the radially orientated electric field lines. Particles with high mobility (small particles) move with a higher velocity toward the column than particles with low mobility (large particles), as Eq. 2.2 shows. Since the velocity in axial direction (dependent on the applied sheath flow rate) is equal for all particles, and the velocity in radial direction depends only on particle size, by default particles of different size will deposit at different locations along the rod. Given that each particle size is attracted toward a different axial point on the centre rod, having a small slit in the rod enables to select a certain size of particles, as shown in the figure. From the slit, the particles are then carried to the outlet, giving a monodisperse aerosol (i.e., consisting of single sized particles).

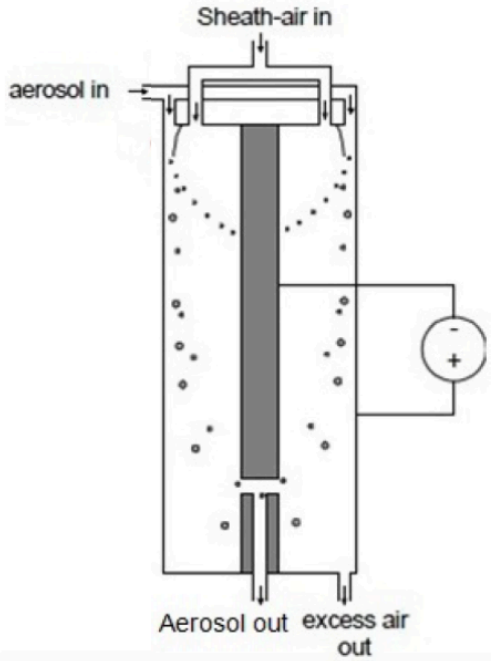

Fig. 2.4. Schematic of a DMA: Polydisperse particles enter and monodisperse particles exit (Obaidullah, Bram, & De Ruyck, 2018).

Nanoparticles are highly diffusive, meaning that they exhibit random motions in the air due to the bombardment by gas molecules (Brownian motion, explained in Section 3.1.1). The high diffusivity of particles at nanoscale makes it difficult to constrain equally sized particles to follow the same path toward the same slit in the DMA. This especially poses a problem when using conventional DMAs (which are mostly used for micron sized particles), because they are larger and involve quite some travelling distance. Therefore, in this work a high resolution (also referred to as half-mini DMA) was used, that is overall smaller and allows much higher sheath flow settings. These high sheath flows, together with small travelling distance make it possible to accurately size-select particles that have diameters as small as an atom (Ude & de la Mora, 2005).

The relation between particle electric mobility Z_p and the operating conditions (i.e., sheath flow rate, Q_S, and voltage, V, applied to the DMA is given by:

$$Z_p = \frac{\kappa Q_S}{V}, \qquad \textbf{(Eq. 2.4)}$$

where κ is the calibration constant of the DMA, that has to be experimentally determined by using particles having a known mobility. In this way, particle size can be tuned by changing the flow rate and the voltage (Ude & de la Mora, 2005).

2.2.4 DMA Calibration

The half-mini DMA was calibrated using tetraheptylammonium bromide (THAB) ions. Same-charge ions are produced using the electrospray technique (also referred to as electro-hydrodynamic atomization). The electrospray method enables a constant production of aerosolized positively charged ions (Maisser, 2011). The electrical mobility of THB^+ ions has been accurately determined and can be found in literature, which therefore serves as calibration standard for the DMA (Ude & de la Mora, 2005). Fig. 2.5 shows the ion concentration as a function of the applied DMA voltage. The DMA voltage is directly related to particle size according to Eqs. 2.3 in 2.2. Therefore, each peak corresponds to a particle size. The peaks shown result from the monomer and the dimer of THAB. Since the sizes of these ions are known, the calibration constant κ for the half-mini DMA (Eq. 2.4) could be determined by reading the voltage of the (monomer) peak at different sheath flows (Q_S). In total, two DMAs were calibrated in this way. Given that the monomer has a mobility of 0.971 m^2/Vs, it follows from Eq. 2.4 and Fig. 2.6 that the κ-values of DMA-1 and DMA-2 are respectively 4.614 and 4.745.

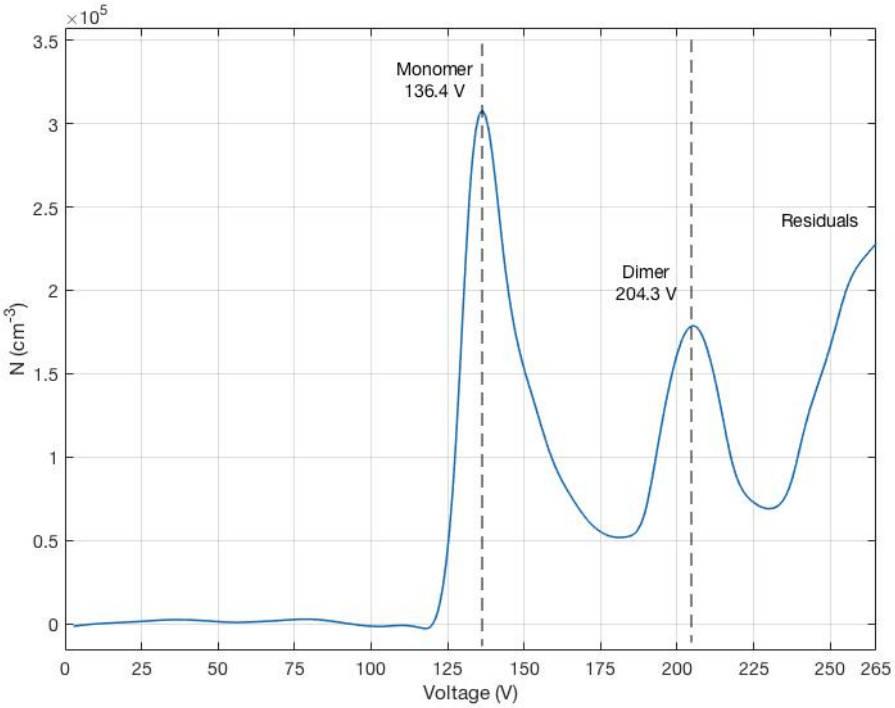

Fig. 2.5. Ion number concentration as a function of the voltage applied to the central rod of the DMA, Q_S = 105 lpm.

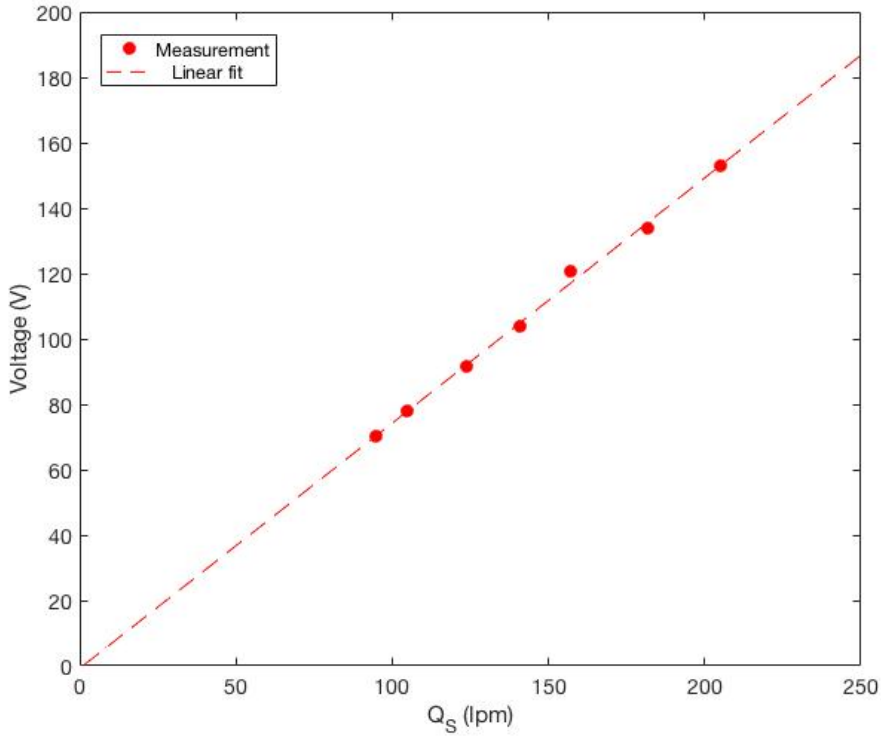

Fig. 2.6. Calibration curve of DMA voltage at monomer peak vs. sheath flow rates. The calibration yields the κ-value intrinsic to each DMA, that is needed for mobility calculations (Eq. 2.4).

3. Bubbling Columns for Nanoparticle Collection

3.1 Introduction

For determining the dissolution rate of nanoparticles that are produced in the gas-phase, it was necessary to develop a technique for collecting particles from the gas to the liquid in a controlled manner, without having the particles agglomerate significantly. It is hereby important to know the fraction of particles that are collected, i.e. the efficiency of the collector. For this purpose, a bubbling column was built, which was subsequently characterized.

3.1.1 Bubbling columns

When a gas enters a column of liquid through little holes, bubbles are formed. If the gas is an aerosol containing nanoparticles, a fraction - if not all - of the particles will deposit on the gas-liquid interface of the bubble (see Fig. 3.1). As a result, particles are passed from the gas phase into the liquid phase.

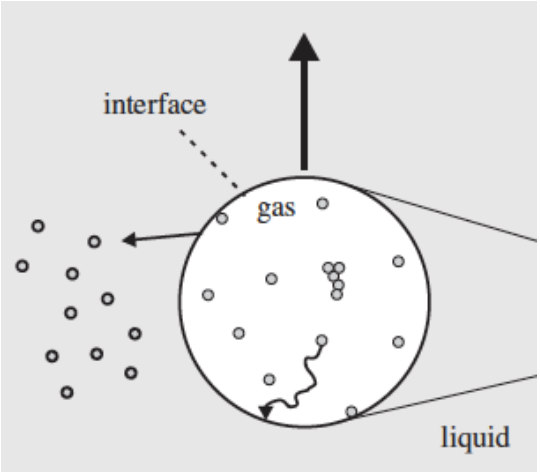

Fig. 3.1. Schematic of particle deposition inside a rising bubble (Koch & Weber, 2012).

Brownian motion

When the bubble contains nanoparticles, their movement toward the interface is primarily caused by diffusion. Particles, particularly the ones in the nanoscale, undergo the so-called Brownian motion: i.e., particles move in an irregular, wiggly manner due to random collisions with gas molecules. Each of the gas-particle collision transfers momentum toward the particle, causing it to change velocity in an irregular and unpredictive manner, as illustrated in Fig. 3.2. The precise particle movement might be unpredictable. However, the net movement is indeed predictable and can be expressed as the particle diffusivity D_B [m^2/s], given by:

$$D_B = \frac{kTC_C}{3\pi\eta d_p} . \qquad \textit{(Eq. 3.1)}$$

Here k is Bolzmann's constant, T is the absolute temperature, C_C is the Cunningham slip correction factor, η is the kinematic viscosity of the gas.

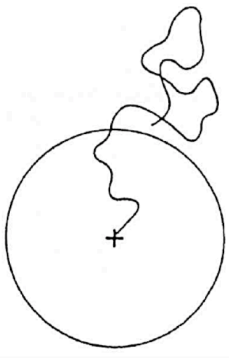

Fig. 3.2. Representation of Brownian motion: projection of the path of a spherical particle's centre of mass (Hinds, 1999), caused by random collisions with gas molecules.

As Eq. 3.1 indicates, the diffusivity is inversely proportional to the particle diameter. Therefore, the bubbling technique works especially well for nanosized particles, for which the diffusivity is high. Through diffusion, these particles cover largest distance in the same amount of time than larger particles, and are therefore more likely to reach the wall of the bubble as this ascends to the surface of the solution.

Once the particle touches the wall of the bubble, it will "stick" and remain there by the attraction of Van der Waals forces, similar to fine chalk sticking to a chalkboard. Once the bubble reaches the top of the water column, it pops and a fraction of the particles theoretically remain in the water.

3.1.2 Theoretical collection efficiency

Pich and Schütz (1991) developed a model that allows for calculations of the theoretical collection efficiency of a bubbling column regarding all sizes of particles from nanoscale to microscale. In this model, the collection efficiency of particles is modelled using the assumption that the mechanism for particle deposition is Brownian diffusion, gravitational settling and inertial impaction inside the bubble (see Fig. 3.3).

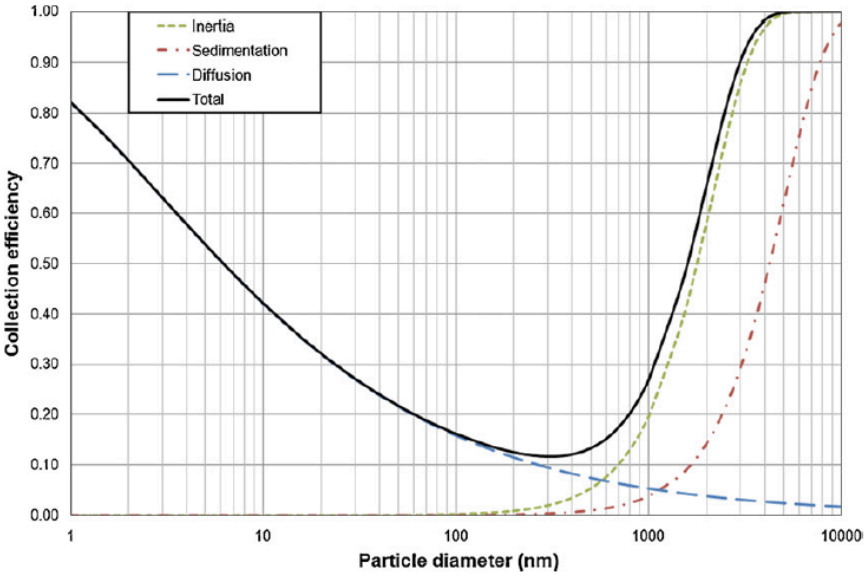

Fig. 3.3. Collection efficiency determined for a bubble of 4 mm diameter and a bubbling depth of 20 cm (Charvet, Bardin-Monnier, & Thomas, 2011).

From Fig. 3.3 it becomes clear that the main mechanism involved in particle collection by bubbling columns of particles with $d_p < 100$ nm is diffusion. Since the particles considered in the frame of this work have diameters in the range around 10 nm, the experimentally determined collection efficiency will be compared to an entirely diffusion-based model. Such model has been developed by Charvet et al. (2011) and it goes as follows.

The average time that it takes for a particle to reach the interface of the bubble depends on the size of the bubble that it is trapped inside. It is therefore necessary to know the size of the bubble. Gaddis and Vogelpohl (1986) constructed the following equation to determine the bubble size (d_b) based on the size of the small holes (d_0), from which the bubbles emerge:

$$d_b = \left[\left(\frac{6 d_0 \sigma}{\rho g}\right)^{4/3} + \left(\frac{81 \nu Q_0}{\pi g}\right) + \left(\frac{135 {Q_0}^2}{4\pi^2 g}\right)^{4/5}\right]^{1/4}, \qquad \textit{(Eq. 3.2)}$$

where σ is the surface tension, ρ is the density of the liquid, ν is the kinematic viscosity and Q_0 is the flow rate. The number of particles initially in the bubble ($N_{p,i}$) with particle number concentration (C_p) is calculated with

$$N_{p,i} = \frac{\pi {d_b}^3}{6} C_p \, . \qquad \textit{(Eq. 3.3)}$$

The root-mean-square displacement (I) of the particles due to Brownian diffusion is then:

$$I = \sqrt{2 D_B t}\,, \qquad \textit{(Eq. 3.4)}$$

where the Brownian diffusivity (D_B) is given by Eq. 3.1, and the time (t) that the bubble takes to reach the surface is:

$$t = \frac{\delta}{U_b}\,, \qquad \textit{(Eq. 3.5)}$$

where δ is the depth of the diffuser, t is the time for the bubble to reach the surface and U_b is the rising velocity of the bubble. The rising velocity of a bubble in water is according to Pich and Schütz (1991) only related to the volume (V_b) of the bubble, according to:

$$U_b = 2.4 {V_b}^{1/6} \qquad \textit{(Eq. 3.6)}$$

If the displacement (I) of the particles inside the bubble is higher than the bubble radius (d_b), then it can be assumed that they have reached the wall of the bubble, hence captured by the water. Therefore, the particles that remain inside the bubble are those that were initially at a distance from the interface that is higher than I. The remaining number of particles in the bubble ($N_{p,f}$) - the ones that escape the bubbler and are not captured - is therefore:

$$N_{p,f} = \frac{4}{3}\pi \left(\frac{d_b}{2} - I\right)^3 C_p \qquad \textit{(Eq. 3.7)}$$

The theoretical efficiency (η_{dp}) at which particles with specific size are collected in the water therefore is:

$$\eta_{dp} = \frac{N_{p,i} - N_{p,f}}{N_{p,i}} \qquad \textit{(Eq. 3.8)}$$

3.2 Experimental

3.2.1 Nanoparticle bubbling

In this study, the collection efficiency was determined for different particle sizes d_p (ranging from 3.5 to 12.5 nm) and different depths δ at which the diffuser is immersed into the water (1, 4 and 7 cm). A different diffuser depth gives a different residence time of the bubble inside the water and different particle sizes have different diffusivities, hence they are expected to have an influence on the collection efficiency.

The bubbling column consists of a glass bottle filled with 400 mL water, an inlet and an outlet. The inlet is a metallic tube with a 3D printed diffuser at the bottom (see Fig. 3.4) and bubbles are created by small holes in the diffuser. The depth of the diffuser can be tuned by sliding the inlet tube up and down.

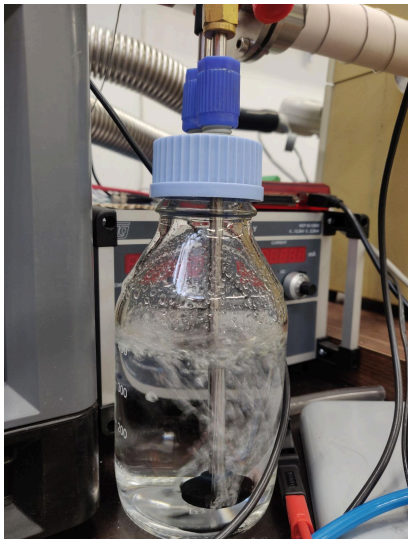

Fig. 3.4. Photograph of the bubbling system in operation, with the diffuser at the bottom, from which bubbles emerge.

Fig. 3.5 shows a schematic layout of the setup for determining the bubbling efficiency for different particle sizes and bubbling depths (δ). Two main routes that were separately used can be distinguished in the setup: Route 1 for measuring the size distribution of monodisperse and polydisperse particles; route 2 for the bubbling measurements. After production of nanoparticles by the Spark Discharge Generator (SDG), the particles were directed through a tube oven that was set to 750 °C. High temperatures cause particles to melt from their agglomerated state into spherical particles, which is referred to as particle sintering. In all of the following experiments, only sintered (spherical) particles are used, because it has several advantages: Firstly, their size can be more accurately determined and selected by the DMAs, because the drag force experienced by sintered particles only depends on particle size is not influenced by any random particle shape. As explained in section 2.2.3 this drag force is important for accurate size selection in the DMA. Secondly, for determining the dissolution rate in relation to particle size (see Chapter 4), it is important that the particle surface area is equal for same sized particles.

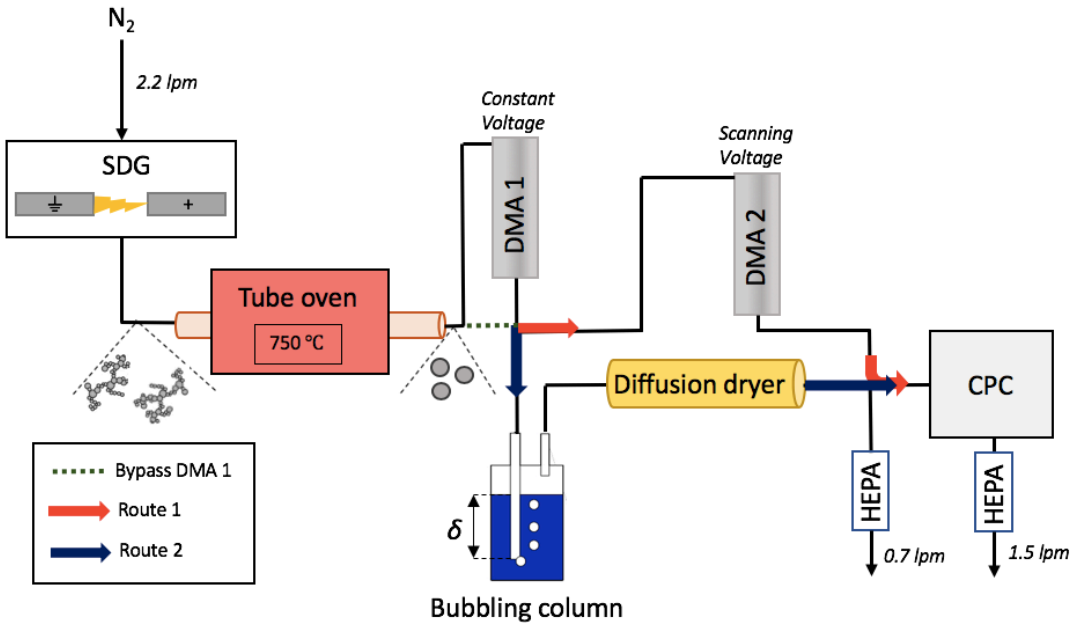

Fig. 3.5. Route 1 (red) shows the size distribution measurements and route 2 (blue) shows the bubbler in operation, where depth δ is adjustable.

Route 1

Using a tandem-DMA (tDMA) setup, monodisperse particles were selected by a first, constant-voltage DMA, followed by the measurement of their size distribution by a second, scanning-voltage DMA in combination with a CPC. Settings on the first DMA for consecutive size selections are: 68 V, 140 V, 234 V, 354 V, 495 V, 660 V and 850 V, which together with a sheath flow of 25 lpm gave the respective monodisperse distributions depicted in Fig. 3.6. Measurement of the larger, polydisperse size distribution (also shown in the same figure) was obtained by bypassing the first, size selecting DMA, as shown in Fig. 3.5. Settings of the spark generator were Q_A = 2.2 lpm, 10 mA,1.3 kV.

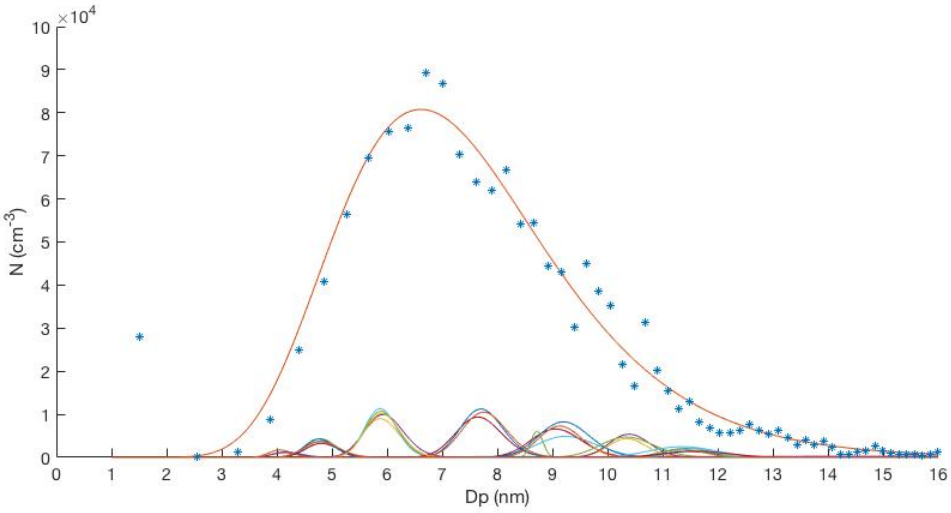

Fig. 3.6. Polydisperse together with multiple monodisperse size distributions. The latter were obtained by keeping the voltage of the DMA constant at different values.

Route 2

The bubbler was placed directly downstream the constant voltage DMA, so that the size distributions determined from route 1, depicted in Fig. 3.5, could be directly bubbled into the water. Two bubbler settings can be distinguished: the diffuser dipped into the water (at a depth δ) and dipped out of the water. From both these settings the respective average number concentrations were measured with the CPC: $N_{in}(\delta)$ (diffuser dipped in water) for different depths and N_{out} (diffuser dipped out of the water). A diffusion dryer was placed downstream the bubbler to ensure that all water particles that might have been created during the bubbling process are removed.

It is desirable to know the concentration of the aerosol particles right before and right after the bubbling column, so that the ratio defines the bubbling efficiency. In practice, however, this is not possible. Before the aerosol reaches the CPC, a considerable length of tubing has to be passed by the aerosol. Aerosol particles, especially those having sizes in the nanoscale, tend to deposit on the inner walls of tubing by diffusion. Particle loss in the tubing is therefore inevitable, which interestingly depends only on the length of tubing and not on the width (assuming the flow is laminar and the deposition is purely by diffusion). Fig. 3.7 shows the modelled particle losses over the length of tubing, using the Gormley and Kennedy model (Gormley & Kennedy, 1948; Hinds, 1999). The figure shows that particle losses are significant for particle sizes below 10 nm for similar lengths of tubing used in the setup (50-70 cm). Since both N_{in} and N_{out} (diffuser dipped in and out of the water respectively) include the same particle losses toward the tubing and the dryer, these losses cancel out once the difference is taken. What remains is the concentration of particles absorbed by the water:

$$N_{abs}(\delta) = N_{out} - N_{in}(\delta) \qquad \textit{(Eq. 3.9)}$$

By dividing the absorbed particle concentration by the initial particle concentration upstream the bubbler ($N_{initial}$), the bubbling efficiency is then:

$$\eta(\delta) = \frac{N_{abs}(\delta)}{N_{initial}} = \frac{N_{out} - N_{in}(\delta)}{N_{initial}} \qquad \textit{(Eq. 3.10)}$$

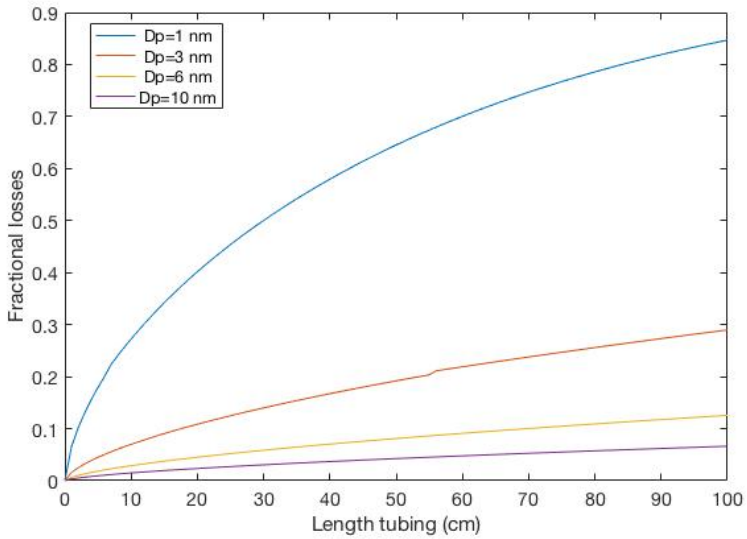

Fig. 3.7. Fractional losses due to diffusion of 1-, 3-, 6- and 10-nm particles on the tubing walls based on the Gormley and Kennedy equations. The calculations were performed using a flow rate of 2.2 lpm at standard conditions (T = 293K, p=1E5 Pa). The length of tubing in the experiment after size selection ranged from 50 to 70 cm.

3.2.2 Nanoparticle sintering

In order to establish whether particles downstream of the tube oven have indeed sintered into spherical particles, an experiment was carried out in which the size of monodisperse particles was measured at the outlet of the tube oven at different temperatures. Agglomerates are classified as larger by a DMA than sintered particles. Thus, by measuring their change in size at different temperatures, it can be established whether the particles are spherical or fractal (Ku & Maynard, 2006). As Fig. 3.8 shows, the size of the particle does not continue to decrease above temperatures of 250 °C, which builds trust that the particle is has indeed sintered into a sphere.

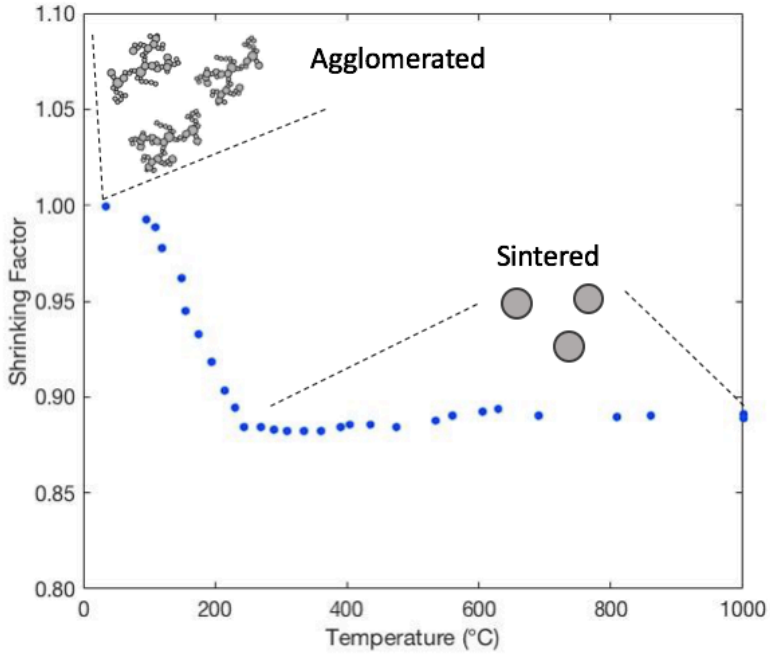

Fig. 3.8. Particle shrinking factor at different temperatures of the tube oven, using monodisperse particles with initial d_p = 8.5 nm. Particles are assumed to be sintered at temperatures above 250 °C.

3.3 Results and Discussion

Fig. 3.9 shows the determined collection efficiencies for three different bubbling depths. Collection efficiencies increase as bubbling depth increases, which is in accordance with the theory. Due to the particle's longer residence time in the bubble at increased depths, more time is available for their diffusion toward the bubble interface. Moreover, the experimental collection efficiency clearly decreases as the particle diameter increases, owing to their lower diffusivity. As can be seen in the figure too, is that the experimental collection efficiency is around 10-30% higher than the modelled collection efficiency. A possible explanation is the following:

During the bubbling, it was observed that besides the large bubbles (which are visible in Fig. 3.4 and from Eq. 3.2 are assumed to have a dimeter of 3 mm), also miniscule bubbles formed. These miniscule bubbles were estimated by eye to have a diameter of < 1 mm and swirled around inside the water for a significantly longer time than the large bubbles. The formation of

these bubbles might have been the result of the slightly porous structure of the 3D printed diffuser, allowing bubble formation not only at the relatively large gaps, but also through the porous material structure itself. The porous structure has significantly smaller holes, and as Eq. 3.2 shows, the size of the bubble depends on the size of the hole. Another reason for the formation of these significantly smaller bubbles might be the vigorous conditions prevailing inside the bubbler that could cause bubbles to break apart into smaller bubbles. Having a fraction of such miniscule bubbles in the bubbler has a direct effect of on the collection efficiency: firstly due to shorter travel distance of particles to reach the bubble interface and secondly due to longer residence times of the bubbles inside the water (Eq. 3.2 and 3.5).

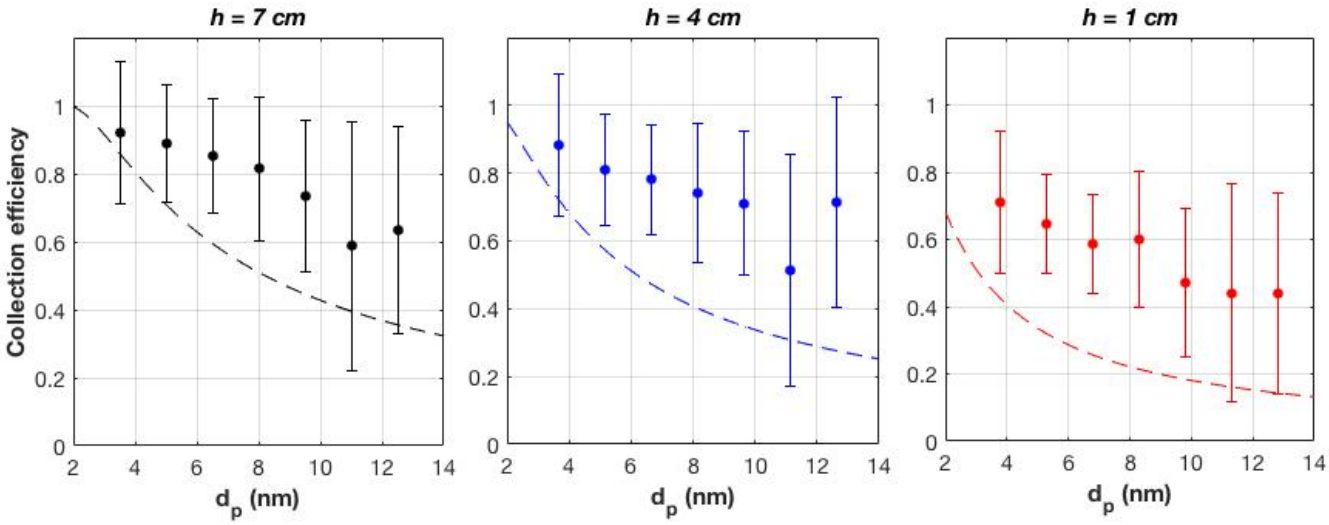

Fig. 3.9. Theoretical (dashed line) and measured collection efficiency vs. particle diameter for different bubbling depths δ.

While bubbling, a yellow stain of nanoparticles gradually formed on the glass bottle, as shown in Fig. 3.10. Since this stain was at water level during the bubbling, it can be hypothesized that (a fraction of) particles that have deposited on the interface inside the bubble end up on the water surface after the bubble pops, from where they migrate toward the glass surface. Since these particles are not collected in the water, it shows a deficit in the method of bubbling: this phenomenon impairs the overall bubbling efficiency.

Both the model and the experimental setup do not account for these types of particle losses against the wall of the vessel, since the efficiency is determined from the fraction of particles entering and leaving the bubbling system. This stain therefore shows that an improvement is needed for both the model and the experimental setup to accurately describe the collection of particles toward the water. The precise fraction of deposited particles and particles inside the water is unknown.

A method to determine the bubbling efficiency in a more precise way - accounting for particle deposition on the vessel - could be to use soluble nanoparticles (e.g. ammonium sulphate) and measure the electrical conductivity of the liquid before and after bubbling. The electrical conductivity can then be directly related to concentration. Comparing the concentration of particles in the aerosol to the concentration of ions in the liquid would therefore give a more direct measure of the particle uptake by the water. One could also use nanoparticles made of salt that has a colour to determine the concentration. The concentration is herein related to the absorbance of light, which can be measured with a UV-Vis.

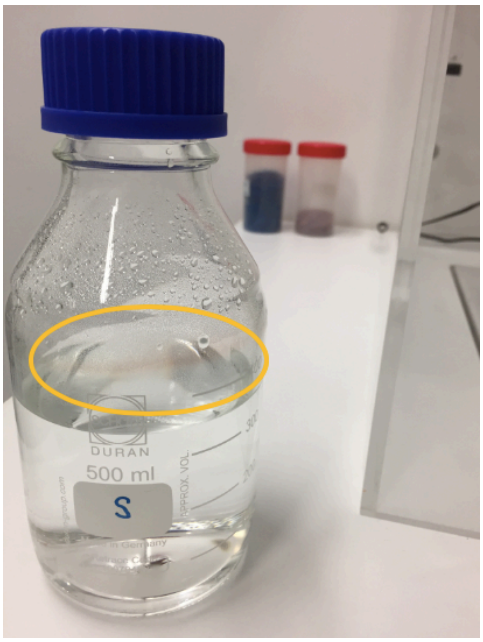

Fig. 3.10. Stain of nanoparticles visible after 1 hour of bubbling with polydisperse particles. At the moment of bubbling, the stain is at water level.

3.4 Conclusions

It is shown that a bubbling column effectively captures nanoparticles of sizes between 3.5 and 12.5 nm. The efficiency at the maximum depth of the diffuser of 7 cm ranges from 60% for the largest to 95% for the smallest particles, indicating that the mechanism of collection is indeed strongly related to the difference in diffusivity of different particle sizes. It could also be shown that the collection efficiency strongly depends on the depth at which the diffuser is dipped in the water.

It is also shown that the bubbling method is not the ideal method for collecting particles in water, because evidently particles deposit against the wall of the vessel instead of being taken up by the liquid. This artefact makes it impossible to know the concentration of particles that are captured in the water with the current method used, in which the concentration of the aerosol was compared before and after the bubbling column.

4. Dissolution Kinetics of Silver Nanoparticles

4.1 Introduction

4.1.1 The principals of nanoparticle dissolution

The dissolution of a solid is a dynamic process, during which atoms migrate from the solid through a diffusion layer into the liquid, as shown in Fig. 4.1. The concentration gradient between the solid surface and the liquid acts as a driving force, either for the migration towards the liquid (dissolution), or the other way around towards the solid (precipitation).

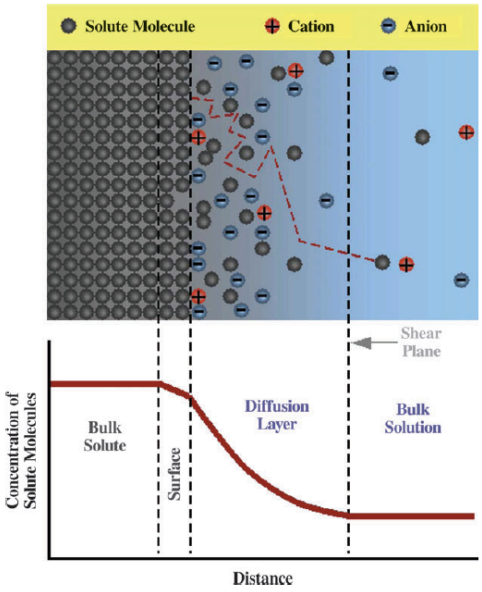

Fig. 4.1. Representation of the dissolution of any material, with the concentration profile of solute molecules as function of distance (Borm et al., 2006).

Solubility

The solubility of the solid (solute) quantifies to what extent the ionic form of the solute is taken up by the solvent. The maximum concentration of solute that the solvent can hold is herein defined as the solubility, expressed in [mg/L]. Solubility depends on the solute itself, but also on the solvent, the composition of the solvent (i.e. pH, oxygen concentration, ionic strength, etc.) as well as the conditions (i.e. temperature and pressure). In the case of salts such as NaCl, the ionic bonds of Na^+ and Cl^- are easily torn apart by the solute: the dipole charge of water molecules pulls with greater forces on the atoms than the ionic bonds in the salt crystal do, and thus the salt ions enter the liquid provided that saturation has not been reached.

Dissolution rate

It is important to realise that the "dissolution rate", which is the measured parameter, depends on both the solubility and available surface area of the solute (Dokoumetzidis & Macheras, 2006). It is expressed in mg/s, and it changes over time due to saturation effects or other effects such as the gradual consumption of limiting chemicals (as will be explained is the case for the dissolution of nanoparticles). Hence, a substance with low solubility doesn't necessarily dissolve slower than a substance with high solubility, given that its exposed surface area is higher. In the case of nano-silver - where silver itself has a significantly lower solubility than salt - dissolution can be measured, mainly resulting from the immense surface-to-volume ratio.

Oxidative dissolution

The dissolution of silver nanoparticles, whose atoms experience metallic bonding as opposed to ionic bonding in salts, dissolution is generally thought to be driven from a fundamentally different mechanism, namely from "oxidative dissolution". It is believed that the oxidation of surface atoms of nanoparticles enables them to dissolve. The dissolution of AgNPs therefore undergoes two stages: firstly, the oxidation of $Ag_{(s)}$ and secondly the dissolution of the oxidised silver, for which protons (H^+) are consumed:

$$4Ag_{(s)} + O_2 \rightarrow 2Ag_2O_{(s)} \qquad \textbf{(Reaction 1)}$$

$$Ag_2O_{(s)} + 2H^+ \rightarrow 2Ag^+ + H_2O \qquad \textbf{(Reaction 2)}$$

Reaction 1 and 2 can be summarized as:

$$4Ag_{(s)} + O_2 + 4H^+ \rightarrow 4Ag^+ + 2H_2O \qquad \textbf{(Reaction 3)}$$

From these reactions it becomes clear that both the oxygen concentration and pH play a critical role in the dissolution kinetics of nanoparticles and are therefore a limiting factor that can cause the particles to dissolve only partially. In various studies, the consumption of one of these two is made responsible for gradual decrease of dissolution rate over time (Zhang et al., 2011).

Fernando and Zhou (2019) also argue that the concentration of H^+ not only affects the dissolution kinetics in a direct manner, but it also has a strong influence on agglomeration kinetics, which in turn influences the dissolution kinetics due to less available surface area. Increased agglomeration kinetics arise from the phenomenon that a change in H^+ concentration influences the surface charge of the particles, which therefore experience a different attraction toward each other. Hence, the dissolution kinetics are not only directly, but also indirectly affected by the pH, which gives an idea of the complexity of nanoparticle dissolution.

Reaction 3 is used in models to predict the ion release kinetics to estimate the dissolution kinetics of the nanoparticles (Zhang et al., 2011). The rate of ionic silver release (γ_{Ag+}) is herein described as:

$$\gamma_{Ag^+} = \frac{3}{4}\left(\frac{8\pi k_b T}{m_B}\right)^{1/2} \rho^{-1} \exp\left(\frac{-E_a}{k_b T}\right) r^{-1} [O_2]^{0.5} [H^+]^2 [Ag]\,, \qquad \textbf{(Eq. 4.1)}$$

where T is the absolute temperature, m_B is the molecular weight of the reactant silver, k_B is the Boltzmann constant, E_a is the activation energy, ρ is the density of AgNPs, r is the radius of the particles, [H^+] and [O_2] are the molar concentrations of dissolved oxygen and hydrogen and [Ag] is the mass concentration of silver. It has to be noted, that the parameters included in the above model mainly represent the dissolution from the chemical point of view, and do not include most of the physical mechanisms that also play a significant role in the dissolution kinetics, as will be discussed in the following paragraphs.

Other parameters affecting the dissolution of nanoparticles

Fig. 4.2 provides an overview of other parameters that have been found to affect the dissolution rate of nanoparticles. It is important to take these effects into account when doing dissolution studies, as each of these has to be kept constant if one wants to measure the effect of a single parameter, such as particle size.

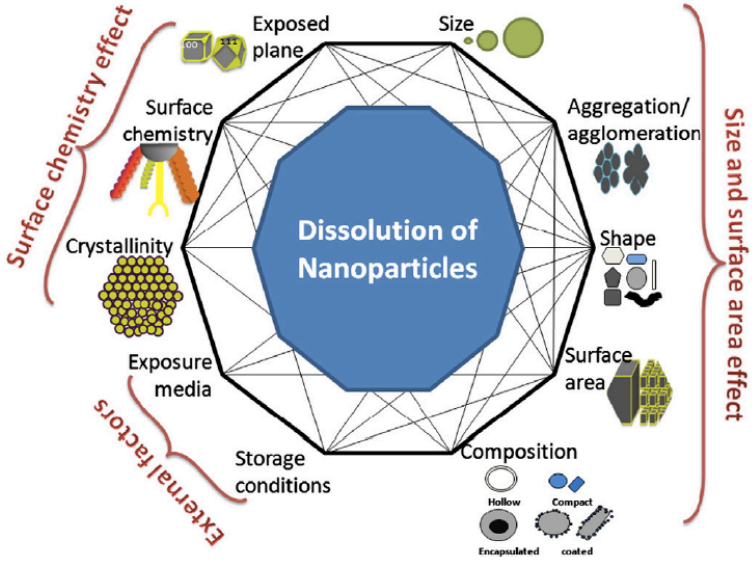

Fig. 4.2. Factors influencing the dissolution kinetics of nanoparticles (Misra, Dybowska, Berhanu, Luoma, & Valsami-Jones, 2012).

To start with, crystallinity contributes to the internal stability of the particle and hence to the dissolution kinetics. Liu, Aruguete, Jinschek, Rimstidt, and Hochella (2008) showed that nanoparticles having differently structured crystals exhibit different dissolution behaviour. Besides, the shape of the particle greatly influences the dissolution rate. Misra, Dybowska, Berhanu, Croteau, et al. (2012) showed that spherical CuO NPs dissolve significantly faster than rod-shaped ones. Storage conditions, such as exposure to light are believed to influence dissolution kinetics. Zhou, Liu, Stallworth, Ye, and Lenhart (2016) compared the dissolution rate of nanoparticles exposed to light and to dark and observed a difference (which can be explained by plasmonic resonances occurring in the particle that is exposed to light). Another factor that is often disregarded, yet it is important, is the state of the diffusion layer (or local saturations) that surrounds a nanoparticle, as shown in Fig. 4.1. This concentration gradient can be increased by, for example stirring the suspension. In a similar way, sugar dissolves faster in water once stirred. Surface chemistry plays a major role, which undergoes dynamical change depending the medium that the particle is surrounded by. As previously described, an important chemical change in the surface layer arises from the reaction with dissolved oxygen, but also other chemicals as chlorine or sulphur play an important role (Zhang et al., 2011). Furthermore, the presence of a surfactant that binds to the particle's surface has inhibiting effects on its dissolution (Misra, Dybowska, Berhanu, Luoma, et al., 2012).

Furthermore, particle size is thought to be an important component affecting the dissolution kinetics of nanoparticles. Partly due to its difference in surface-to-volume ratio, but also due the particle's changed intrinsic physical properties in the nanoscale. The overall binding energies in nanoparticles are weaker than those in bulk matter, even so weak that particles below a threshold size exhibit liquid behaviour (Buffat & Borel, 1976). Particle size can also have a rather indirect effects on the dissolution rate. For example, particle size influences the agglomeration rate inside the liquid (since Brownian diffusivity changes with size), which in turn has an effect on the exposed surface area, hence on the dissolution. Although, this effect was shown to be minimal in measurements carried out by Zhang et al. (2011), who concluded that the primary particle size rather than the aggregated size is responsible for ion release kinetics, it can play a role at higher AgNP concentrations. Also, a different particle size (or even the method of formation) can affect the particle's crystal structure, which in turn affects the dissolution rate (Castleman Jr & Khanna, 2009; Grassian, 2008).

4.1.2 Previously determined dissolution constants

The rate of ion release of a particle can be defined in terms of the dissolution rate or dissolution constant k (h^{-1}). Note that owing to its unit, the absolute quantity of dissolved matter is disregarded, as it cancels out in the formula for determining the dissolution rate (as will be shown further on). An important thing to mention is that complete AgNP dissolution has not been observed in the large majority of the previous studies. It has been shown that particles dissolve until they reach an equilibrium size, from where further dissolution does not occur. Since this partial dissolution can have many reasons (seen the large number of influencing factors), a clear understanding for this incomplete dissolution has not been found and the reason is only speculated in literature.

Table 4.1 shows the dissolution constants determined in previous studies. In all of the studies, Ag particles were synthesized by the wet-chemistry techniques. With this method, nanoparticles are produced by chemical means, formed from precipitation reactions. When using the wet chemical synthesis, surfactants are needed to keep particles in the suspension stable. The surfactant forms a stable organic layer around the particle, which enables characterization of the produced nanoparticles (such as size, concentration or crystal structure) without them starting to dissolve or to agglomerate. Dissolution of the particles starts once the stock solution is diluted to a sufficient degree, such that the concentration of the surfactant is thought to be low enough to remove the coated layer, hence destabilizing the particle.

Table 4.1. Nanoparticle dissolution rates found in literature together with the experimental settings.

Study	d_p (nm)	$[Ag]_{total}$ (mg L^{-1})	Surfactant	Other added compounds	Temperature	pH	Measurement method	$k_{dissolution}$ (h^{-1})
Liu and Hurt (2010)	4.8 ± 1.6	0.05-2.00	citrate	5mM boratec buffer	Room temperature	4-8	AAS**	**0.0100 – 0.0252**
Zhang et al. (2011)	20 40 80	0.300 (0.600)	citrate	Hoagland medium	25 °C	5.6	ICP-MS***	**0.0147** **0.0258** **0.0555**
Peretyazhko, Zhang, and Colvin (2014)	6 9 13	8.0	PEG*	none	Room temperature	7	Silver selective electrodes, TEM† and UV-Vis	**0.0517** **0.0179** **0.0062**
Hui, O'Dell, Rao, and Riley (2019)	4.8 ± 1.6	1.00	citrate	Lactic acid, urea, NaCl	Room temperature	4.5-5.5	Linear sweep voltammetry	**0.0168 – 0.1524**
Kittler, Greulich, Diendorf, Köller, and Epple (2010)	46 ± 5	140 320	citrate	none	25 °C	N.A.	AAS	**0.0170** **0.0210**
Zhou, Liu, Stallworth, Ye, and Lenhart (2016)	76.7	1.52 (dark) 1.17 (light)	none	NaNO3	Room temperature	7	ICP-OES ††	**0.0019** **0.0055**

*Polyethyleenglycol; ** Atomic Absorption Spectroscopy; *** Inductively Coupled Plasma Mass Spectrometry; † Transmission Electron Microscopy; †† Inductively Coupled Plasma Optical Emission Spectrometry

The use of a surfactant has the advantage that the nanoparticle suspension is kept stable and can be stored for a considerable amount of time without particles changing their morphology or chemistry. However, a drawback is that the use of surfactants adds impurities to the liquid and to the surface of the nanoparticles, which can influence the dissolution rate.

Nanoparticles used in this thesis are produced in a fundamentally different way, namely from the gas phase. Compared to previous methods, this enables the measurement of nanoparticle dissolution rates without the use of surfactants or added chemicals. At the same time, synthesizing the nanoparticles in the gas phase enables selection of monodisperse particles with an extremely high precision using the high-flow DMA (see Section 2.2.3). This precise size selection makes it possible to accurately determine the influence of particle size on dissolution

kinetics. Besides, the spark ablation method enables the production of particles that have high purity throughout. By adding oxygen to the carrier gas, it is even possible to create particles with a constant oxidation level from surface down to the core of the nanoparticle. As Reaction 3 shows, oxidation is one of the driving parameters for dissolution and can heavily influence the kinetics.

4.2 Experimental

Preparation of mother solution

Nanoparticles that are produced by the spark discharge were effectively collected in water using the bubbling method (Chapter 3). Prior to bubbling, the particles passed through a tube oven, in which they were sintered, giving them a spherical shape. As mentioned before, making sure that the nanoparticles have a spherical shape is important in order to exclude shape-related influences on particle dissolution, as well as making it possible to determine the surface-to-volume ratio. The setup used for particle collection is essentially the same as the one shown in Fig. 3.5. As the collection efficiency has been established for each particle size in Section 3.3, the quantity of collected particles in the solution after bubbling over a specific amount of time can be established.

In this experiment, the effect of different sizes on the dissolution rate will be established. Hence, different suspensions were made containing different sizes of monodisperse particles. It is important to exclude any differences in surface-to-volume ratio, because dissolution rates may cause saturation to be reached at different extents, or may cause differences in availability of O_2 or H^+ for the different sizes, since these chemicals are the main limiting factors as described previously. Ensuring an equal surface concentration when preparing nanoparticle suspensions with different particle diameter was done as follows:

The total surface area A of n nanoparticles with diameter d_p (nm) is:

$$A = 4\pi \left(\frac{d_p}{2}\right)^2 n \,. \qquad \textit{(Eq. 4.2)}$$

The number of nanoparticles captured in suspension during time t (min) is:

$$n = Q\, t\, N\, \eta_{d_p} \,, \qquad \textit{(Eq. 4.3)}$$

where Q is the flow rate (L/min), N is the number concentration (dm^{-3}) and η_{dp} is the size-dependent collection efficiency (-) that has been determined (Chapter 3).

Substituting Eq. 4.3 into Eq. 4.2 and accounting for the volume of water U (L) gives the total surface concentration $[A]$ collected in the water in (nm^2/L):

$$[A] = \frac{\pi\, {d_p}^2\, Q\, t\, N\, \eta_{d_p}}{U} \,. \qquad \textit{(Eq. 4.4)}$$

The surface concentration is kept constant by bubbling for a different amount of time (t) for each suspension of different d_p. N was kept constant, since changing N would involve changing the production rate from the spark generator, which could introduce artefacts resulting from different intrinsic properties (such as different crystallinity). Other factors that might have an effect on the dissolution rate were kept constant to the degree that this was possible.

Preparation of ICP-MS samples

After having collected the particles inside the water, samples were prepared for the measurement of Ag^+ concentration with Inductively Coupled Plasma Mass Spectrometry (ICP-MS). ICP-MS is a type of mass spectrometry that is able to detect metals at concentrations down to 1 ppt (0.001 µg/L). The liquid is herein atomized, after which the water evaporates, solidifying all ions that were in solution into particles (Ammann, 2007). Through inductive heating of the carrier gas (Argon), these particles are then heated to up to temperatures high enough for ionizing the solid, which creates a plasma consisting of electrons and all types of positively charged ions. The positive ions are selected based on their mass-to-charge ratio. The induced signal from the selected ions is linearly related to the concentration of the substance. A main advantage of using an ICP-MS for dissolution studies is its significantly lower detection limit compared to other types of ion concentration measurements. A disadvantage is that it is an off-line measurement that involves high maintenance and costs.

The measurement of Ag^+ concentration over time with the ICP-MS gives a direct measure of dissolution rate. The method of preparing samples for the ICP-MS measurement is depicted in Fig. 4.3 (route a). As described above, the nanoparticles were bubbled into the mother solution. At different time intervals, samples were taken from this mother solution and were subsequently filtered (Amicon Ultra-4 centrifugal membrane filter, 4 kDa pore size), removing all nanoparticles from the solution. The filtrate therefore contains only the silver ions (Ag^+) that dissolved during the period between particle collection in the bubbler and the moment of filtering. Thus, taking samples and filtering them at different time intervals enables the measurement of the change of [Ag^+] over time. The dissolution rate can then be determined using these measurements. All of the samples were digested in 2% HNO_3, in order to remove possible silver ion complexes and to guarantee that no nanoparticles are present, which can damage the ICP-MS. This procedure was done for each size and the dissolution of nanoparticles was recorded over a total period of 10 days.

Fig. 4.3 (route b) shows the method in which the total concentration of nanoparticles initially present in the liquid was determined. This was done by skipping the filtering step and digesting the nanoparticles instead with a 10% HNO_3 solution, which gives the total silver concentration, namely [Ag^+ + AgNP]. Knowing the total concentration, it is therefore possible to determine the percentage of dissolved particles.

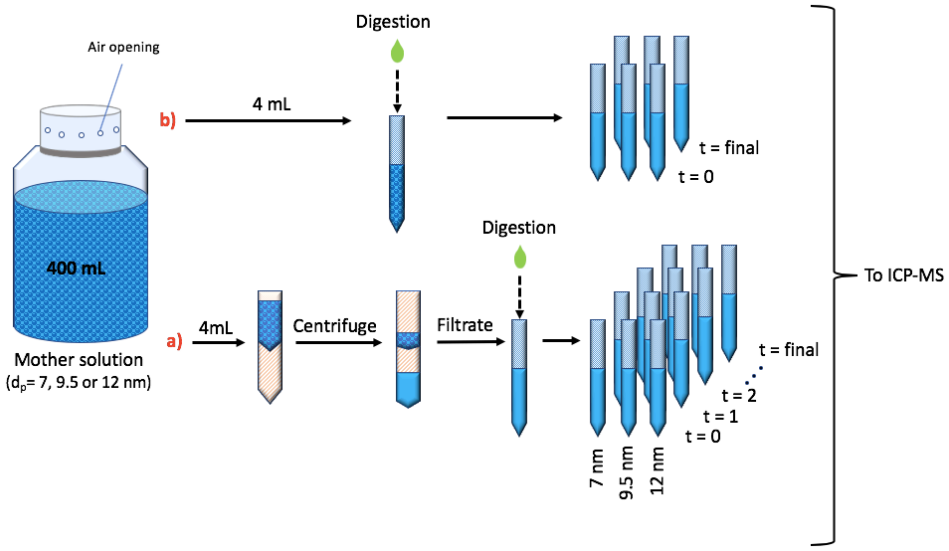

Fig. 4.3. Overview of ICP-MS sample preparation method. Samples from the mother solution were either filtered (a) or not filtered (b), corresponding to the measurement of [Ag^+] and [Ag^+ + AgNP], respectively, after digestion. An air opening was kept in the mother solution bottle to allow the passage of oxygen, which might be consumed by the oxidative dissolution.

4.3 Results and Discussion

4.3.1 Curve fitting

To compare Ag^+ release kinetics with other studies, it is necessary to calculate the kinetic parameter k (h^{-1}) using the empirical kinetics equation developed by (Kittler et al., 2010), which is expressed as:

$$[Ag^+]_t = [Ag^+]_{final}(1 - \exp(-kt)) \,, \qquad \textit{(Eq. 4.5)}$$

where $[Ag^+]_t$ (µg/L) is the silver ion concentration measured at time t and $[Ag^+]_{final}$ is the silver ion concentration in equilibrium.

Since dissolution already starts during particle collection by bubbling (i.e., during preparation of the total mother solution), this prior dissolution has to be accounted for. A simple way of doing that is to make a small modification to Eq. 4.5, introducing the term t_0:

$$[Ag^+]_t = [Ag^+]_{final}\big(1 - \exp\big(-k(t - t_0)\big)\big) \,, \qquad \textit{(Eq. 4.6)}$$

Fig. 4.4 shows the obtained $[Ag^+]$ concentrations from the ICP-MS measurements. As it seems, the data is highly dispersed and it is difficult to fit Eq. 4.6.

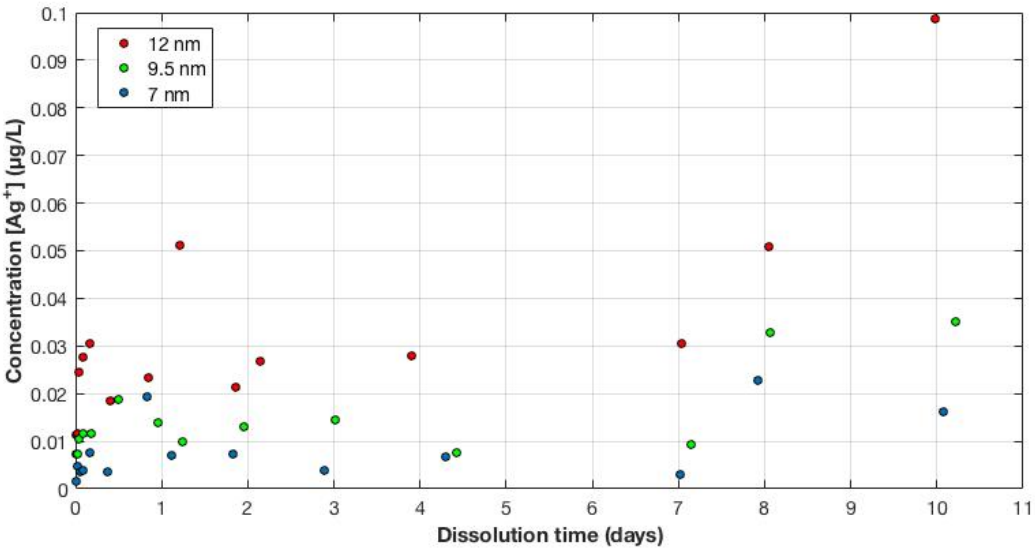

Fig. 4.4. Raw data of ICP-MS concentration measurements of $[Ag^+]$ versus the elapsed dissolution time.

The high scattering of the measurements indicates that something has gone wrong during the experiment, which makes it challenging to fit any type of line through the data. Following reasoning could explain the highly scattered results:

The ICP-MS measures the concentration of Ag^+ by taking small samples from plastic falcon tubes, of which each tube has a different time stamp (as depicted in Fig. 4.3a). Each of these falcon tubes represents one data point in Fig 4.4. These falcon tubes were newly purchased,

marked as sterilized, therefore they were rinsed 3 times with milli-Q water before use. Making sure that the tubes are clean is important, because impurities can cause the formation of silver ion complexes, according to following general reaction (Anderegg, 1992):

$$Ag^+ + X \leftrightarrow AgX^+, \qquad \textit{(Reaction 4)}$$

where X is a ligand capable of forming a complex with Ag^+. This reaction is known to have a high equilibrium constant, indicating that it goes strongly to the right-hand side. In the presence of ligands (impurities), Ag^+ is therefore prone to form a complex, and the limiting factor are these impurities. These ion complexes can deposit on the surface of the falcon tube. Silver that has deposited on the falcon tube will therefore not be measured by the ICP-MS. Different degrees of impurities thus yields different degrees of ion complex formation and hence causes random errors in each sample.

The presence of impurities in the tube was observed: during vortexing the falcon tubes, a thin layer of foam formed on the surface, which was also observed when vortexing with pure milli-Q water. The formation of foam was not observed after thoroughly cleaning these tubes with soap. The foam therefore indicates impurities that come directly from the newly purchased falcon tubes. Apparently, the rinsing procedure that was done at the beginning was not sufficient to remove all of the impurities. Having impurities in each falcon tube, of which the degree of contamination depends on the extent of the rinsing, it can be assumed that ion complex formation has occurred in each tube at different degrees, yielding different Ag^+ concentrations measured by the ICP-MS.

In order to try and fit the exponential function of Eq. 4.6, a method was followed for selecting only the valuable data points for the fit. The main consideration of the methods is that there is always the possibility that among the contaminated tubes there are some in which the contamination is insignificant or systematic. By the definition of dissolution, the ion concentration increases over time. Therefore, the concentration of the n^{th} selected data point is necessarily higher than the concentration of the n-1^{th} selected data point, where n increases with time. In other words, only data points that are higher than the previous selected value are included in the fit:

$$[Ag^+]_n > [Ag^+]_{n-1} \,. \qquad \textit{(Eq. 4.7)}$$

Fig. 4.5 shows the fit, in which data points were excluded according to the above methodology. The respective fitting parameters of each curve are shown in Table 4.2. Despite the low number of data points that the fit goes through, which makes its precision questionable, a qualitative conclusion can be drawn, namely that that particles of small diameter reach equilibrium concentrations faster than large particles. This finding is consistent with previous measurements, for example those of Peretyazhko et al. (2014), adding some trust to the method of fitting and overall to the measurements carried out in this work.

Table 4.2. Parameters of Eq. 4.6 including dissolution constant k obtained from the fitting with 95% confidence interval.

d_p	$[Ag^+]_{final}$ (µg/L)	t_0 (d)	k (h^{-1})	R-square fit
12 nm	0.0991	0.437	0.0195	0.963
9.5 nm	0.0338	0.234	0.0473	0.990
7 nm	0.0229	0.0504	0.0837	0.991

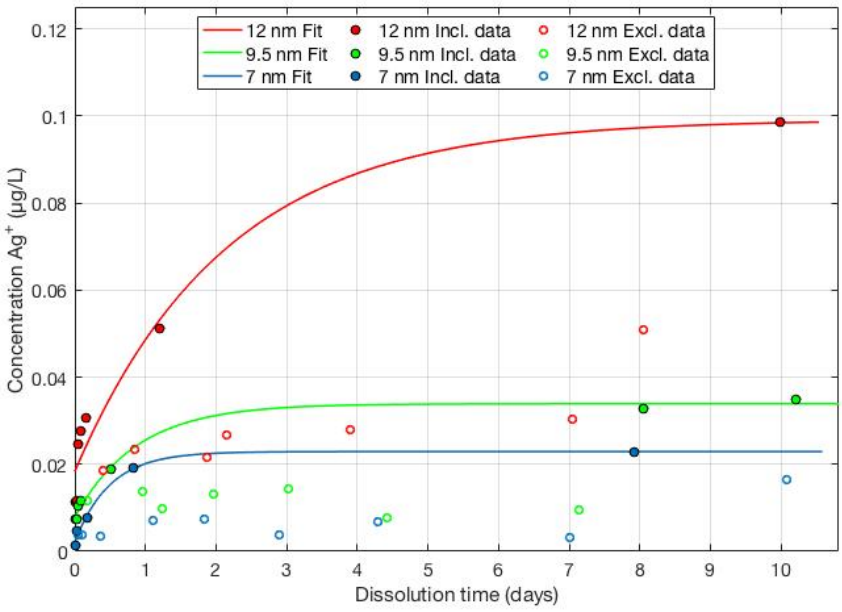

Fig. 4.5. Exponential fits through the adjusted measurements of [Ag^+] over time. Included and excluded data points are indicated with a cross and a circle respectively.

4.3.2 Interpretation

Given the fact that it is possible to make an exponential fit, it can be assumed that the errors of the data points included in the fit are mainly of systematic nature. According to Eq. 4.6, only the relative concentrations of Ag^+ (µg/L) are relevant for determining the dissolution constant *k*: this value is related to the ratio of $[Ag^+]_t$ and $[Ag]_{final}$ at equilibrium, thus any systematic error cancels out. This means that impurities in the tubes of the selected data points must have either been approximately equal (assuming that the degree of impurity is linearly related to this systematic error) or absent. Note that with this reasoning, the equilibrium Ag^+ concentrations respective to particle size are meaningless, since the systematic error for each size is unknown. The only conclusion to be drawn is the difference in time that is needed to reach equilibrium for each size, and the calculation of *k* itself.

To draw a conclusion whether the dissolution is complete or incomplete, the total concentration of nanoparticles was measured (see Table 4.3). This was done both at the beginning, $[Ag]_{tot,i}$, and at the end after 10 days, $[Ag]_{tot,f}$, by digesting all nanoparticles with 10% HNO_3 without filtering them out first, which gives [Ag^+ + AgNP]. This procedure is depicted in Fig. 4.3b in the methods section. The measurements in the table show unequal concentration of total silver at the beginning and at the end, which is not realistic. This indicates that silver, in any form, is deposited on the walls, which made it impossible to be sampled by the ICP-MS.

Table 4.3. Total silver concentration in the bottle $[Ag]_{tot}$, defined as [Ag^+ + AgNP] in the beginning $[Ag]_{tot,i}$ and after 10 days $[Ag]_{tot,f}$. Multiple samples were taken, allowing the calculation of RSD.

d_p	$[Ag]_{tot,i}$	$[Ag]_{tot,f}$
12 nm	0.030 µg/L (83.3 %)	0.340 (3.6 %)
9.5 nm	0.034 µg/L (27.1%)	0.208 (0.7 %)
7 nm	0.026 µg/L (82.3%)	0.127 (4.6 %)

Two possible reasons for silver depositing on walls are:

a) AgNPs adhered to the walls of the glass vessel directly after being bubbled in the solution, dissolving from there and therefore causing $Ag_{tot,f}$ to be higher than $Ag_{tot,i}$. Visual inspection of the bottle indeed showed depositions on the vessel (see Fig. 3.10). The percentage of nanoparticles adhering to the glass bottle is unknown, however. Thus, the influence of this effect cannot be quantified.

b) The other explanation arises from ion complexes that deposit on the wall of the falcon tubes, as this is assumed to be an important factor for inaccuracies in this experiment. The samples of $[Ag]_{tot,i}$ were standing around in the lab for around 10 days before being measured, whereas $[Ag]_{tot,f}$ was measured relatively soon after being sampled. This means that for both cases there is a difference in time available for the formation, deposition and possibly precipitation of silver ion complexes, explaining why $[Ag]_{tot,f} > [Ag]_{tot,i}$. Moreover, as shown Table 4.3, the standard deviation of $[Ag]_{tot,i}$ is significantly higher than that of $[Ag]_{tot,f}$, which could underline the different extents of deposition that has happened over time.

Fig. 4.6 shows the dissolved percentage of AgNP over time for each size, which was obtained by taking the ratio between $[Ag^+]_t$ and the total concentration $[Ag]_{tot,f}$. As it seems from the graph, 12 nm particles reach higher equilibrium concentrations than smaller particles, which is not in agreement with theory. From theory and observation in previous studies, smallest particles are expected dissolve to the greatest extent.

Note that due to possible inaccuracies in the measurement of $[Ag]_{tot}$, owing to the same reasoning of the formation of silver ion complexes in the falcon tube, the percentage comes with a random error. This random error can be explained by the nature of calculating the percentage:

$$\%\ AgNP\ dissolved = \frac{[Ag^+]_{t,d_p} \pm \sigma_1}{[\mathrm{Ag}]_{tot,d_p} \pm \sigma_2} \cdot 100\% \,. \qquad \textit{(Eq. 4.8)}$$

This ratio involves the division of two unknown systematic errors σ_1 and σ_2, which are different for each size d_p. Hence, the resulting percentage has a different (random) error for each size. This makes it difficult to quantitatively compare the dissolved fraction of the nanoparticles presented in Fig. 4.6. A faulty calculation of the dissolved percentage could therefore explain that 12 nm dissolves to the greatest extent, despite the expectation that it should dissolve slowest compared to the other sizes. A quantitative conclusion about the dissolved fraction of particles can therefore not be drawn, and it is therefore unknown if the particle dissolved fully or only partially. In the following, it is assumed that particles dissolve only partially, because this has been repeatedly observed in literature.

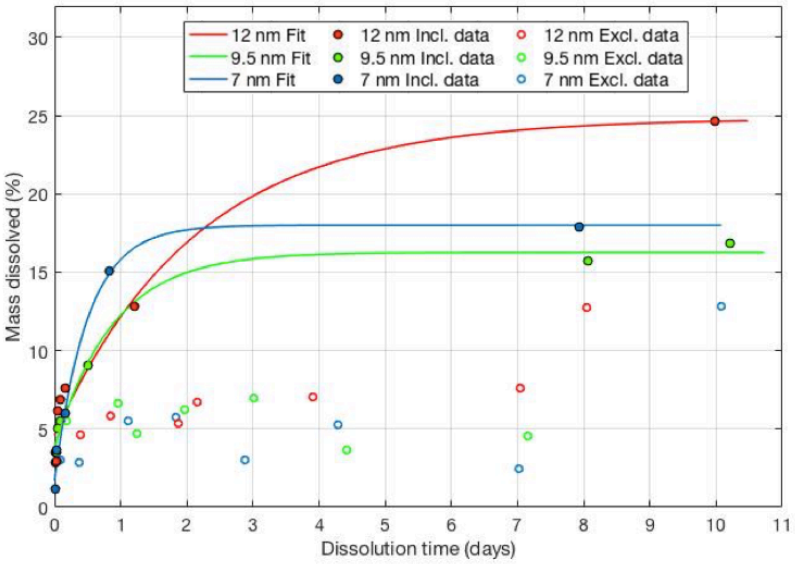

Fig. 4.6. Exponential fits through the dissolved percentage of AgNPs. Included and excluded data points are indicated with a cross and a circle respectively.

4.3.3 Comparison of k-values

Fig. 4.7 shows the dissolution constant as obtained from the fits, together with those from previous studies. It shows that the order of magnitude agrees with measurements found in literature. Note, that the concentration of nanoparticles used in this experiment is 2-4 orders of magnitude lower than the concentrations in previous experiments, yet yielding a dissolution constant *k* that is comparable, which is astounding. The number of experiments relating particle size to dissolution rate is limited, nevertheless the dissolution constants from this study show high correspondence with the ones obtained by Peretyazhko et al. (2014). In their study, nanoparticles were produced from the liquid phase by chemical reduction reactions and subsequently the particles were stabilized with polyethyleenglycol (see table 4.1). Nanoparticle concentrations in their study were as high as 8 mg/L, whereas concentrations of monodisperse particles used in this study are 4 orders of magnitudes lower, around 0.1 µg/L.

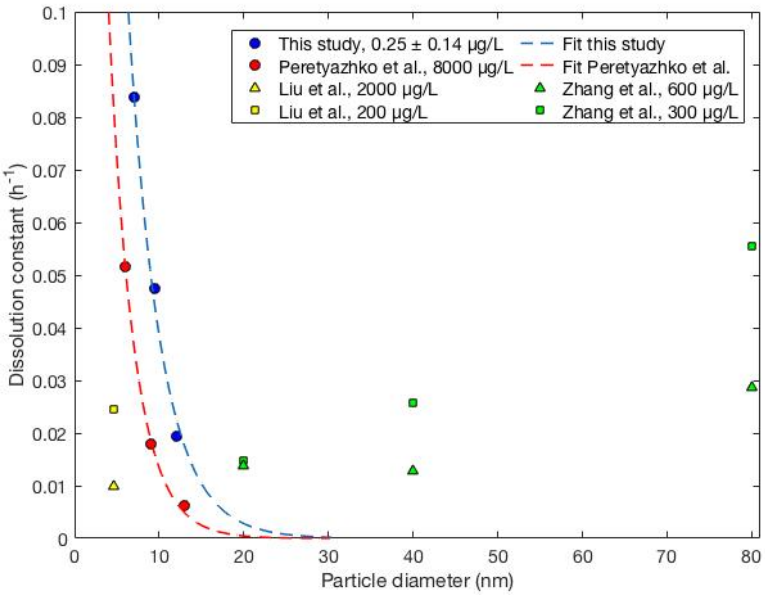

Fig. 4.7. Comparison of dissolution constants (k) for varying particle sizes found in literature with different initial AgNP concentrations.

Seen the large agreement between Peretyazhko et al. (2014) and this study despite the tremendous AgNP concentration difference of 4 orders of magnitude, gives reason to believe that *k*, at this span of concentrations, is only weakly dependent (or even independent) to nanoparticle concentration.

Other studies have focused on the effect of nanoparticle concentration on dissolution kinetics and do find much more pronounced relationships between *k* and concentration. In the study of Liu and Hurt (2010), a decrease of AgNP concentration by a factor of 10 causes the dissolution rate to increase by a factor of 2.46. Kittler et al. (2010) showed that with similar concentration drops the dissolution rate increases by a factor of 5.40. Zhang et al. (2011) also observed a size dependency on this influence of concentration, in which the dissolution of small particles is less influenced by concentration changes than large particles (see Fig. 4.7; distance between green triangles and squares decreases at lower *dp*).

Explanations given by the authors for this concentration dependence are saturation effects that might become significant for higher nanoparticle concentrations, or the depletion of chemicals like H^+ and O_2, since these are the main limiting factors contributing to oxidative dissolution (see reaction 3). These explanations do not agree with observations from this study: when comparing the current study with the one of Peretyazhko et al. (2014), the large agreement of dissolution constants - despite the enormous concentration difference between the current study indicates that saturation effects did not occur significantly. The same can be said about the availability of H^+ and O_2, as previously explained. Apparently, in the range of the used concentrations of nanoparticles from 0.1 μg/L (current study) to 8000 μg/L (their study), these factors haven't reached their limiting effect yet. These observations therefore indicate that nanoparticle concentration does not significantly affect the dissolution constant at these concentrations.

The dependence of *k* on concentration observed in the previous studies could be explained given the fact that all of these studies use surfactants, which are known to affect the surface chemistry of nanoparticles. This is the reason that they are used in the first place: to stabilize nanoparticles so that they don't dissolve before starting the experiment. At low enough concentrations, it is believed that the stabilizing effect disappears, in which case particles dissolve. However, the surfactants could in principle still have a direct influence on the dissolution kinetics even at low concentrations, since their preferred state is being bound to the particle's surface. The strong relation of *k* to nanoparticle concentration from previous studies could therefore be explained by following:

If the concentration of nanoparticles is changed by dilution, then the concentration of surfactant present in the liquid is automatically changed, too. This could yield different dissolution kinetics due to differences in surfactant concentration, and not due to differences in nanoparticle concentration. Moreover, the observation made by Zhang et al. (2011) that smaller sizes are less affected by concentration changes, could be explained by a similar reasoning: smaller particles have a larger total surface area at equal nanoparticle (mass) concentrations compared to larger particles. Therefore, smaller sizes are less influenced by equal amounts of surfactant than larger sizes. Using surfactants, it could therefore *look as if* smaller particles are less influenced by changes in AgNP concentration. This discussion point was not raised by the authors. In the study of Zhang et al. (2011), stock solutions of citrate coated nanoparticles were purchased, which contain equal concentrations of surfactant for each size. Different concentrations of AgNPs were obtained by a simple dilution of the stock liquid, not accounting for the ratio between available surface area of the nanoparticle and surfactant concentration. In

order to systematically prove the effect of surfactants on dissolution kinetics, however, it would be necessary to make direct comparisons, comparing the dissolution rate of solutions with and without surfactants. This can easily be done with the current method, by introducing a surfactant after collecting particles from the gas phase.

Since in the above argumentation limiting effects such as the consumption of H^+ are put as parameters that have only little to no impact on dissolution, a different explanation is needed. As Liu et al. (2008) concluded, the type of crystal structure of the nanoparticle is relevant to its dissolution kinetics. Fig. 4.8 shows a TEM image that was obtained in their study, which clearly shows that the dissolution doesn't happen uniformly over the surface of the particle. It could therefore be, that dissolution depends on the local weaknesses of the crystal structure within the particle. Only the weak parts of the structure dissolve, keeping the strong ones intact. This could be a more important (particle intrinsic) cause could also explain why that particles reach an equilibrium size, from which they stop dissolving.

Moreover, in a study on the crystal structures of nanoparticles in the gas phase, it was concluded that certain sizes of clusters are more stable than others (Castleman Jr & Khanna, 2009). Clusters containing a certain number of atoms are highly stable and are referred to as the "magic numbers". For example, a gold cluster that exists of 55 atoms (Ag-55) exhibits much more stability than gold clusters of other sizes. The same effect could hold true for a gradually shrinking nanoparticle due to dissolution, where dissolution might stop once an "ideal" number of atoms is present in the crystal structure.

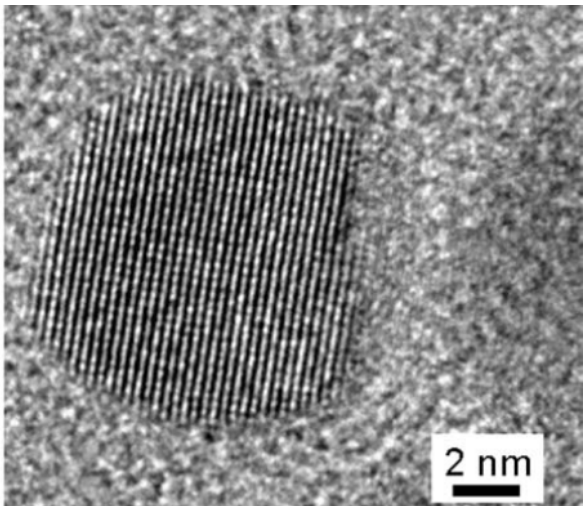

Fig. 4.8. A galena nanoparticle after dissolution (Liu et al., 2008).

Possible size related effect on solubility

An effect that could be responsible for the observation that smaller particles reach equilibrium faster than larger particles could be due to a nano-effect, in which the particle's solubility depends on its size. This sounds counterintuitive, since solubility is defined as the maximum amount of solute that can be taken up by the solvent and intuitively should not depend on the size of the solute. Wu and Nancollas (1998) provided a theory, however, stating that the solubility of particles in the nanoscale could indeed be size dependent. This size-dependency on solubility follows from the difference in (positive) curvature of smaller particles as compared to larger particles. Atoms on a curved surface experience a lower binding energy compared to the atoms on a less curved or flat surface, due to less direct neighbours. Atoms

located on a more curved surface (i.e. small particles) therefore detach easier from the solid into the liquid than atoms on a flat surface. The effect that this has on the solubility is described by the Ostwald-Freundlich relationship:

$$\rho\nu \frac{RT}{M} ln \frac{S_r}{S_\infty} = \frac{2\gamma_s}{r}, \qquad \textit{(Eq. 4.9)}$$

where S_r is the solubility of a particle with radius r, S_0 is the solubility of the bulk material that has a flat surface, γ_s is the surface free energy, ρ is the density of the solid, ν indicates the number of moles of ions that are formed from one mole electrolyte, R is the gas constant and T is the temperature. This effect has not yet been shown experimentally, which could be due to the fact that the dissolution of nanoparticles depends on a large number of mechanisms, from which it is difficult to single out the size-induced solubility changes.

4.4 Conclusions

In this study, the dissolution constant of silver nanoparticles produced from the gas phase was determined. Nanoparticles were transferred from the gas to the liquid using a bubbling column. It is the first time that the dissolution rate was determined from particles from gas phase and several advantages to conventional methods can be distinguished: Firstly, the use of surfactants, which add impurities to the liquid and the surface of the nanoparticles and can possibly influence the dissolution kinetics, can be avoided. Secondly, in-situ methods for determining the size of particles from the gas-phase are advanced, allowing the exact measurement of initial particle size. Third, as compared to the production of nanoparticles from the liquid phase, that are based on precipitation reactions, our method is capable of producing highly monodisperse particles of finely tuned size. This enables the measurement of dissolution in relation to particle size without the occurrence of influencing factors such as Ostwald ripening (smaller particles dissolving before larger ones). Lastly, the production of particles from the gas phase by spark ablation method allows the production of very pure particles. Impurities such as oxidation can be finely tuned by adding oxygen to the carrier gas.

It could be shown that a relationship between particle size and dissolution kinetics exists, although repetition of this experiment is needed to ensure the validity of the result. The pH was not influenced by the dissolution in a measurable way, most probably owing to the low concentration of nanoparticles used. This excludes an important artefact, since pH is known to strongly influence both agglomeration kinetics and dissolution kinetics. In this study it was thus shown, that working at particle concentrations in the range of 0.1 µg/L is advantageous. Observing a dissolution constant that is comparable to one that was obtained by Peretyazhko et al. (2014), in which 4 orders of magnitude higher concentrations were used, adds confidence to believe that the dissolution rate is - at these conditions - not concentration dependent and therefore not influenced by saturation effects or by the consumption of limiting chemicals.

Intrinsic (physical) particle characteristics are hypothesized to be responsible for the observation that smaller particles reach equilibrium faster than large particles. Two of these are changes in differences in crystallinity and differences in particle curvature (Kelvin effect). In order to prove the first, it would be necessary to study the crystallinity in more detail by taking TEM images or XRD before and after dissolution studies. Another way of showing the importance of physical mechanisms is to include sizes that are outside the nanoscale, at which these physical effects are expected to be lower or absent. To prove the physical effect of particle curvature in a direct way, it might be necessary to further decrease the chemical mechanisms that are generally thought to be the main driving force of the dissolution. Once the chemical

mechanisms are decreased or ruled out, the curvature effect is singled out. One way of doing this could be to eliminate the main chemical mechanism - oxidative dissolution - by working at anoxic conditions, or to work with a material that is known not to oxidize (e.g., gold). The main question here is, if dissolution will happen at all. If dissolution is hereby observed, it would validate importance of physical mechanisms at the nanoscale. Near-to anoxic conditions could also be sufficient to observe a distinction between physical and chemical dissolution mechanisms. Such conditions could be achieved with the current setup, by bubbling long enough with pure N_2 such that most oxygen is removed from the water before starting to introduce particles. An oxygen trap might be needed, to ensure the production of pure, oxygen-free nanoparticles. Such measurements, anoxic or at different oxygen concentrations, could bring more insight on the intrinsic dissolution mechanisms. Once the effect of these intrinsic properties on dissolution is better understood, the size-dependent solubility can be finely tuned, in order to achieve controlled dissolution kinetics, which can be adjusted to their application.

Bibliography

Ammann, A. A. (2007). Inductively coupled plasma mass spectrometry (ICP MS): a versatile tool. *Journal of mass spectrometry, 42*(4), 419-427.

Anderegg, G. (1992). Complex formation of silver (I) ion with some aminopolycarboxylate ligands. *Inorganica chimica acta, 194*(1), 31-35.

Benn, T., Cavanagh, B., Hristovski, K., Posner, J. D., & Westerhoff, P. (2010). The release of nanosilver from consumer products used in the home. *Journal of environmental quality, 39*(6), 1875-1882.

Borm, P., Klaessig, F. C., Landry, T. D., Moudgil, B., Pauluhn, J., Thomas, K., Wood, S. (2006). Research strategies for safety evaluation of nanomaterials, part V: role of dissolution in biological fate and effects of nanoscale particles. *Toxicol Sci, 90*(1), 23-32.

Buffat, P., & Borel, J. P. (1976). Size effect on the melting temperature of gold particles. *Physical review A, 13*(6), 2287.

Castleman Jr, A., & Khanna, S. (2009). Clusters, superatoms, and building blocks of new materials. *The Journal of Physical Chemistry C, 113*(7), 2664-2675.

Charvet, A., Bardin-Monnier, N., & Thomas, D. (2011). Can bubble columns be an alternative to fibrous filters for nanoparticles collection? *J Hazard Mater, 195*, 432-439.

Dale, A. L., Casman, E. A., Lowry, G. V., Lead, J. R., Viparelli, E., & Baalousha, M. (2015). Modeling nanomaterial environmental fate in aquatic systems. *ACS Publications.*

Dokoumetzidis, A., & Macheras, P. (2006). A century of dissolution research: from Noyes and Whitney to the biopharmaceutics classification system. *Int J Pharm, 321*(1-2), 1-11.

Fernando, I., & Zhou, Y. (2019). Impact of pH on the stability, dissolution and aggregation kinetics of silver nanoparticles. *Chemosphere, 216*, 297-305.

Friedlander, S. K. (1977). Smoke, dust and haze: Fundamentals of aerosol behavior.

Gaddis, E. S., & Vogelpohl, A. (1986). Bubble formation in quiescent liquids under constant flow conditions. *Chemical Engineering Science, 41*(1), 97-105.

Gormley, P., & Kennedy, M. (1948). *Diffusion from a stream flowing through a cylindrical tube.* Paper presented at the Proceedings of the Royal Irish Academy. Section A: Mathematical and Physical Sciences.

Grassian, V. H. (2008). When size really matters: size-dependent properties and surface chemistry of metal and metal oxide nanoparticles in gas and liquid phase environments. *The Journal of Physical Chemistry C, 112*(47), 18303-18313.

Helmlinger, J., Sengstock, C., Groß-Heitfeld, C., Mayer, C., Schildhauer, T. A., Köller, M., & Epple, M. (2016). Silver nanoparticles with different size and shape: equal cytotoxicity, but different antibacterial effects. *RSC Advances, 6*(22), 18490-18501.

Hinds, W. C. (1999). *Aerosol technology: properties, behavior, and measurement of airborne particles*: John Wiley & Sons.

Hui, J., O'Dell, Z. J., Rao, A., & Riley, K. R. (2019). In Situ Quantification of Silver Nanoparticle Dissolution Kinetics in Simulated Sweat Using Linear Sweep Stripping Voltammetry. *Environ Sci Technol, 53*(22), 13117-13125.

Kittler, S., Greulich, C., Diendorf, J., Köller, M., & Epple, M. (2010). Toxicity of Silver Nanoparticles Increases during Storage Because of Slow Dissolution under Release of Silver Ions. *Chemistry of Materials, 22*(16), 4548-4554.

Koch, D., & Weber, A. P. (2012). Separation of gas-borne nanoparticles in bubble columns. *Journal of aerosol science, 53*, 61-75.

Köhler, H. (1936). The nucleus in and the growth of hygroscopic droplets. *Transactions of the Faraday Society, 32*, 1152-1161.

Ku, B. K., & Maynard, A. D. (2006). Generation and investigation of airborne silver nanoparticles with specific size and morphology by homogeneous nucleation, coagulation and sintering. *Journal of aerosol science, 37*(4), 452-470.

Levard, C., Hotze, E. M., Lowry, G. V., & Brown Jr, G. E. (2012). Environmental transformations of silver nanoparticles: impact on stability and toxicity. *Environmental science & technology, 46*(13), 6900-6914.

Liu, Aruguete, D. M., Jinschek, J. R., Rimstidt, D. J., & Hochella, M. F. (2008). The non-oxidative dissolution of galena nanocrystals: Insights into mineral dissolution rates as a function of grain size, shape, and aggregation state. *Geochimica et Cosmochimica Acta, 72*(24), 5984-5996.

Liu, & Hurt, R. H. (2010). Ion release kinetics and particle persistence in aqueous nano-silver colloids. *Environmental science & technology, 44*(6), 2169-2175.

Maisser, A. (2011). *Investigation and applications of nanoscale biological and inorganic aerosols using electro-hydrodynamic atomization (EHDA) and electrical mobility analysis.* uniwien,

Misra, S. K., Dybowska, A., Berhanu, D., Croteau, M. N., Luoma, S. N., Boccaccini, A. R., & Valsami-Jones, E. (2012). Isotopically modified nanoparticles for enhanced detection in bioaccumulation studies. *Environ Sci Technol, 46*(2), 1216-1222.

Misra, S. K., Dybowska, A., Berhanu, D., Luoma, S. N., & Valsami-Jones, E. (2012). The complexity of nanoparticle dissolution and its importance in nanotoxicological studies. *Sci Total Environ, 438*, 225-232.

Nowack, B., Krug, H. F., & Height, M. (2011). 120 years of nanosilver history: implications for policy makers. *Environ Sci Technol, 45*(4), 1177-1183.

Obaidullah, M., Bram, S., & De Ruyck, J. (2018). An overview of PM formation mechanisms from residential biomass combustion and instruments using in PM measurements. *International Journal of Energy and Environment, 12*, 41-50.

Peretyazhko, T. S., Zhang, Q., & Colvin, V. L. (2014). Size-controlled dissolution of silver nanoparticles at neutral and acidic pH conditions: kinetics and size changes. *Environ Sci Technol, 48*(20), 11954-11961.

Pfeiffer, T. V., Feng, J., & Schmidt-Ott, A. (2014). New developments in spark production of nanoparticles. *Advanced Powder Technology, 25*(1), 56-70.

Pich, J., & Schütz, W. (1991). On the theory of particle deposition in rising gas bubbles: The absorption minimum. *22*(3), 267-272.

Reinmann, R., & Akram, M. (1997). Temporal investigation of a fast spark discharge in chemically inert gases. *Journal of Physics D: Applied Physics, 30*(7), 1125.

Schwyn, S., Garwin, E., & Schmidt-Ott, A. (1988). Aerosol generation by spark discharge. *Journal of aerosol science, 19*(5), 639-642.

TSI Incorporated (2002). Model 3025A Ultrafine Condenstion Particle Counter Instruction Manual.

Ude, S., & de la Mora, J. F. (2005). Molecular monodisperse mobility and mass standards from electrosprays of tetra-alkyl ammonium halides. *Journal of aerosol science, 36*(10), 1224-1237.

Wu, W., & Nancollas, G. H. (1998). A new understanding of the relationship between solubility and particle size. *Journal of solution chemistry, 27*(6), 521-531.

Zhang, W., Yao, Y., Sullivan, N., & Chen, Y. (2011). Modeling the primary size effects of citrate-coated silver nanoparticles on their ion release kinetics. *Environ Sci Technol, 45*(10), 4422-4428.

Zhou, W., Liu, Y. L., Stallworth, A. M., Ye, C., & Lenhart, J. J. (2016). Effects of pH, Electrolyte, Humic Acid, and Light Exposure on the Long-Term Fate of Silver Nanoparticles. *Environ Sci Technol, 50*(22), 12214-12224.